Vol. 35 • No. 16 • April 18 • 2025

www.afm-journal.de

ADVANCED FUNCTIONAL MATERIALS

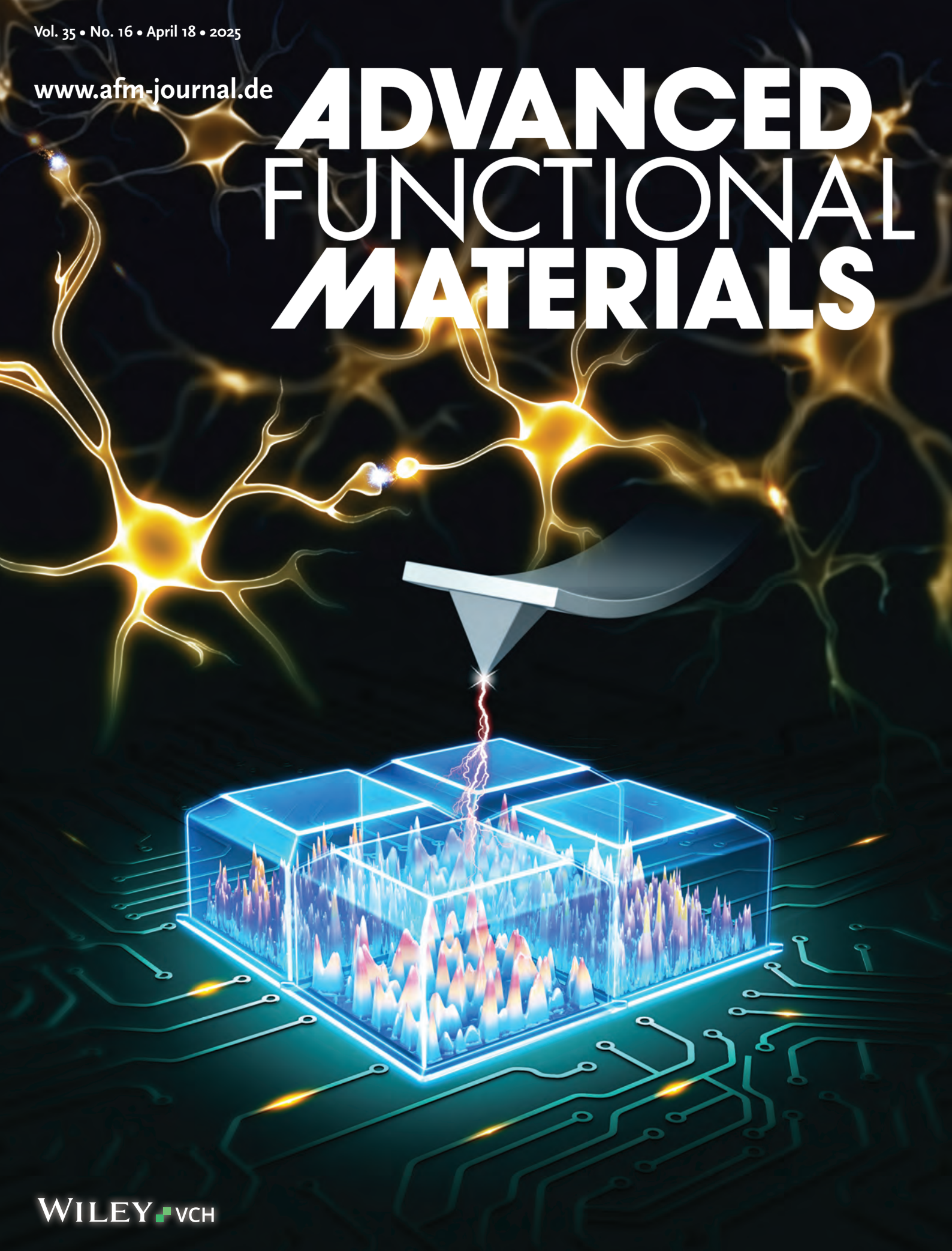

WILEY VCH

ADVANCED FUNCTIONAL MATERIALS
www.afm-journal.de

Phosphorylation Enables Nano-Graphene for Tunable Artificial Synapses

Zhenyu Zhang, Yuanduo Qu, Siran Chen, Shanwu Ke, Mengdi Hao, Yongyue Xiao, Shuai Zhang, Ziqiang Cheng, Jiangrong Xiao, Hao Huang, Cong Ye, Paul K. Chu, Xue-Feng Yu, and Jiahong Wang**

Flexible and robust memristors with controllable resistance-switching characteristics are important to neuromorphic computing. However, the nanomaterials-based, solution-processed resistance switching layer usually has poor reliability and tunability due to uneven morphology and invariable surface properties. Herein, phosphorylated graphene nanoflakes (phos-GPs) are synthesized for high-performance solution-processed flexible memristors. In situ conductive atomic force microscopy reveals that the tightly stacked uniform nanoflakes and modified phosphorate groups jointly reduce the formation barrier of the conductive filaments. Furthermore, phosphorylation gives rise to surface silver ion coordination leading to enhanced radial growth of the conductive filaments. The memristor shows volatile characteristics in the Ag/phos-GPs/ITO architecture and exhibits non-volatile properties in the Ag/Ag^+-(phos-GPs)/ITO structure. Both types of memristors display consistent *I--V* curves during long-term cycling and under repetitive mechanical bending, in addition to excellent synaptic plasticity. Moreover, ultrasmall nonlinearity is observed from non-volatile long-term synaptic potentiation and depression. By utilizing the tunable artificial synapses, the processes of memory-forgetting and re-recognition are simulated, and the image recognition tasks are accomplished by the artificial neural networks.

1. Introduction

Memristors with resistance-switching (RS) characteristics have attracted tremendous attention due to their large storage density and reliability.[1,2] They have been applied to many areas including information storage, artificial intelligence, and telecommunication.[3,4] Moreover, flexible memristors are being explored as artificial synapses in wearable sensors and intelligent textiles.[5,6] 2D materials with variable electronic properties and excellent mechanical flexibility can be used to fabricate the RS functional layer.[7,8] Various methods such as chemical vapor deposition, physical vapor deposition, and atomic layer deposition have been utilized to prepare 2D materials-based memristors. However, the typically high reaction temperature and complex transfer/photolithography limit the practicality and versatility.[9,10] In contrast, solution-processing techniques can be performed

Z. Zhang, Y. Qu, S. Chen, S. Ke, M. Hao, Y. Xiao, S. Zhang, Z. Cheng, H. Huang, X.-F. Yu, J. Wang
Shenzhen Institute of Advanced Technology
Chinese Academy of Sciences
Shenzhen 518055, P. R. China
E-mail: hao.huang@siat.ac.cn; jh.wang1@siat.ac.cn

Z. Zhang, M. Hao
Southern University of Science and Technology
Shenzhen 518055, P. R. China

Y. Qu, X.-F. Yu, J. Wang
Guangdong Provincial Key Laboratory of Multimodality Non-Invasive Brain-Computer Interfaces
Shenzhen 518055, P. R. China

S. Chen, X.-F. Yu, J. Wang
University of Chinese Academy of Sciences
Beijing 100049, P. R. China

S. Ke, Y. Xiao, C. Ye
Faculty of Physics and Electronic Science
Hubei University
Wuhan 430062, P. R. China

The ORCID identification number(s) for the author(s) of this article can be found under https://doi.org/10.1002/adfm.202416794

DOI: 10.1002/adfm.202416794

Z. Cheng
Department of Applied Physics
East China Jiaotong University
Nanchang 330013, P. R. China

J. Xiao
School of Chemical and Environmental Engineering
Wuhan Polytechnic University
Wuhan 430023, P. R. China

P. K. Chu
Department of Physics
Department of Materials Science and Engineering
Department of Biomedical Engineering
City University of Hong Kong
Tat Chee Avenue, Kowloon, Hong Kong, China

X.-F. Yu
The Key Laboratory of Biomedical Imaging Science and System
Chinese Academy of Sciences
Shenzhen 518055, P. R. China

J. Wang
Shenzhen University of Advanced Technology
Shenzhen 518055, P. R. China

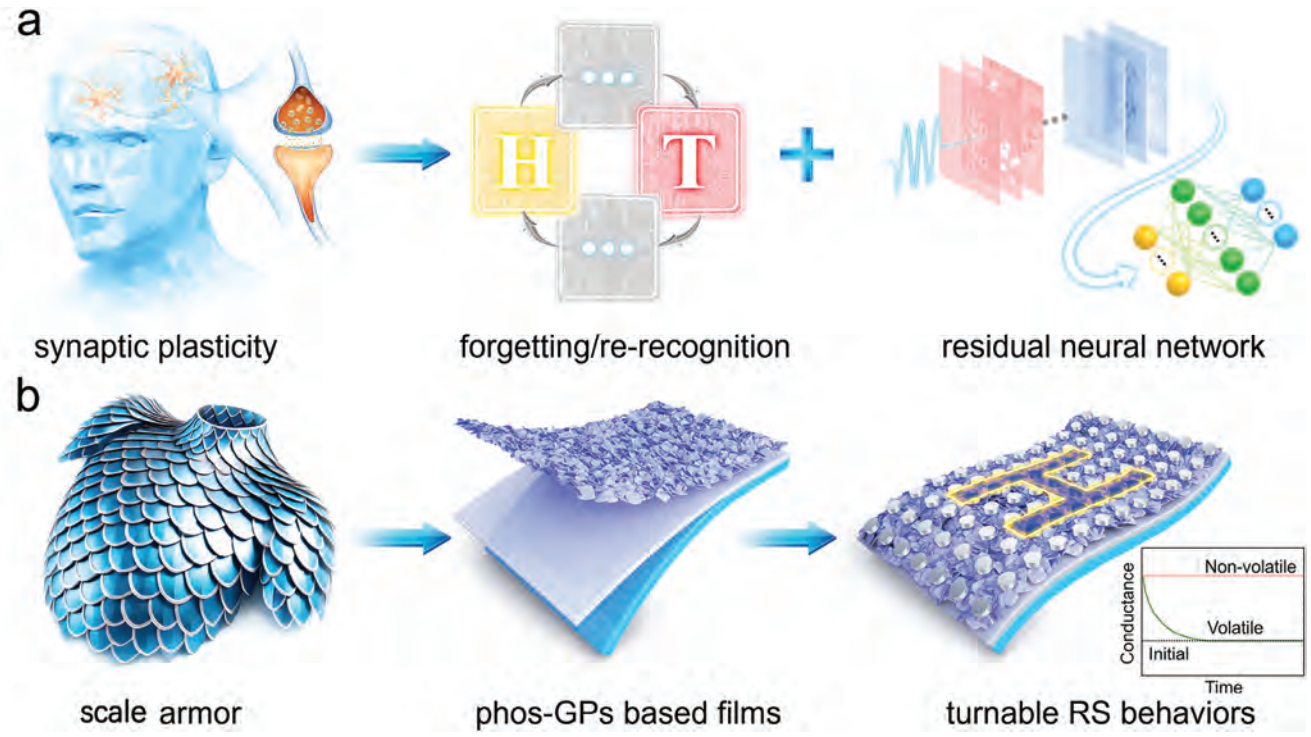

Figure 1. a) Schematic illustration of the synaptic plasticity in the human brain, forgetting/re-recognition function of volatile artificial synapses, and construction of an artificial neural network based on non-volatile artificial synapses; b) schematic illustration of the scale armor structure which inspires the design of phos-GPs based films and memristors.

at a lower temperature that is more compatible with 3D printing or mechanical spraying to produce large-scale integrated devices.[11,12] Although several types of 2D materials including black phosphorus, MoS_2, and MXene have been employed to for the solution-processed RS layers in memristors,[13–15] the uniformity is a critical issue. 2D nanoflake dispersions usually have large size variations, which impact RS layer formation, and improper stacking of 2D nanoflakes can produce micro-holes or nano-cracks.[16,17] The uneven RS layer increases the interfacial traps in the conductive filaments leading to ultimate device failure. Therefore, the synthesis of uniform 2D nanoflakes for solution-processed RS layers is crucial to the development of memristors.

In order to mimic artificial synapses with memristors, conductive mode turnability is another important issue. The volatile or non-volatile properties can be tailored by constructing the proper artificial neural networks (**Figure 1a**). Doping and surface modification are efficient ways for 2D materials,[18,19] for instance, formation of edge defects in small MoS_2 nanoflakes, modification of Ti_3C_2Tx MXene with octylphosphonic acid, and incorporation of organic functional groups (-NH_2, -COOH, -OH) into graphene oxide nanoflakes. These processes can reduce the formation energy of the conductive filaments, modulate the threshold voltage, stabilize the retention time, and enhance the ON/OFF rates.[20–22] However, surface functionalized species tend to have weak polarization, thereby producing weak interactions with the conductive filaments. Additionally, the density of the functionalized groups after post-treatment is often not large enough to cause appreciable effects. Therefore, the development of highly functionalized and uniform-sized 2D nanoflakes is highly desirable to constructing memristors with tunable RS behavior.

Inspired by the structure of scale armor (**Figure 1b**), 2D nanoflakes that can form dense thin films with short-range ordered stacking and chemical interaction while maintaining device-scale flexibility are designed. Due to its superior mechanical and thermal properties, graphene has garnered substantial interest in flexible neuromorphic devices.[23,24] Typically, large graphene oxide nanosheets are applied as the RS layer, in which defects are important for regulating the formation and melting of conductive filaments. Moreover, surface group functionalization serves to enhance the hydrophilicity of the nanosheets, prevent the aggregation of nanoflakes, and modulate the coordination environment of silver ions.[25] Traditional methods of functionalizing graphene surfaces are often complex, involving multiple steps and post-treatments, resulting in low functional density.[26–28] To address this, we propose a red phosphorus-assisted high-energy ball milling strategy to synthesize small phosphorylated graphene nanoflakes (phos-GPs). Furthermore, the well dispersed uniform phos-GPs are applied to fabricate uniform solution-processed films for memristors. Benefiting from the coordination between the phosphate groups and silver ions (Ag^+), the memristors based on phos-GPs can be turned to have volatile or non-volatile characteristics. The artificial synaptic properties and related applications are explored. In particular, simulated memory-forgetting and re-recognition are demonstrated from the phos-GPs-based volatile memristor. The outstanding conductance modulation ability of the

Ag^+-coordinated phos-GPs-based non-volatile memristor is demonstrated, revealing short-term synaptic plasticity (STP) and long-term synaptic depression (LTD) with high linearity. Based on the memristor array, a Residual Network (ResNet) and a deep learning model are used to build an artificial neural network (ANN). This framework successfully accomplishes the Canadian Institute for Advanced Research 10 (CIFAR-10) recognition task and handwritten digit recognition task. The phos-GPs based memristors have high reliability and multifunctional adjustability, and this novel strategy is expected to spur the use of solution-processed 2D materials in next-generation devices.

2. Results and Discussion

2.1. Synthesis of Phos-GPs Nanoflakes

To synthesize phos-GPs with uniform nanosize and stable dispersivity, bulk graphite is first exfoliated by red phosphorus-assisted high-energy ball milling to obtain the phosphorus-modified graphite nanoflakes (Figure S1, Supporting Information). The surface covalently bonded elementary phosphorus is transformed into phosphate groups in a nitric acid treatment. After removing excess phosphorus, the phos-GPs dispersion is produced (**Figure 2**a). Phosphorylation is studied by X-ray photoelectron spectroscopy (XPS). As shown in Figure 2b, the two peaks of P-O and P-C appear at 132.0 and 132.7 eV in the P 2*p* spectrum of phos-GPs. The survey and C 1*s* spectra confirm the existence of P-C bonds in phos-GPs (Figure S2, Supporting Information).[29,30] The phosphorylation-related functional groups including P═O, P-O-P, C-O-P emerge from the FTIR spectrum (Figure S3, Supporting Information) These results indicate that the activated carbon atoms react with red phosphorus to form C-P bonds under the high pressure during ball milling and are further oxidized to C-P(═O)$(-OH)_2$ by nitric acid to complete graphite phosphorylation.[31,32] The exfoliation and nanosizing of phos-GPs nanosheets are investigated by XRD (Figure 2c). Compared to graphite, the (002) peak of phos-GPs is broader and shifts to a lower angle, proving that phos-GPs are exfoliated to form the few-layer structure. In the Raman scattering spectra (Figure 2d), the D and G peaks of phos-GPs are at 1341.7 and 1612.6 cm^{-1}, respectively, while the pristine graphite exhibits the D, G, and 2D peaks at 1355.8, 1580.2, and 2725.4 cm^{-1}. The broadened D and G peaks of phos-GPs, enlarged D/G ratio, and also invisible 2D peak indicate the lattice destruction and surface functionalization of phos-GPs.[33,34] Owing to the efficient surface phosphorylation, the phos-GPs nanoflakes are dispersed well in water (Figure S4a, Supporting Information).

The lateral dimensions and thickness of the phos-GPs are derived from the AFM (Figure 2e) and TEM images (Figure S4b, Supporting Information), the horizontal dimension (50–100 nm) and the thickness (1–4 nm) of phos-GPs nanoflakes are much smaller than the phosphate-functionalized graphene synthesized by other method. (Table S1 and Figure S4c,d, Supporting Information). The phos-GPs nanoflakes via The phos-GPs nanoflakes are dispersed in a solvent with an isopropanol-to-water ratio of 4:6 to produce the dense and flat film by high-speed spin-coating. The uniform size and small thickness allow phos-GPs to assemble into a densely stacked fish-scale armor structure during spin-coating (Figure 2f). The memristors are fabricated by thermal deposition of a top Ag electrode. The cross-sectional view of the phos-GPs film-based memristor (Figure 2g) illustrates that the dense phos-GPs film is almost parallel to the ITO electrode, and the thickness of phos-GPs film is ≈70 nm.

2.2. Volatile Properties of Phos-GPs-Based Memristors

As shown in **Figure 3**a, the phos-GPs thin film is applied as the RS layer, while Ag and indium tin oxide (ITO) form the top and bottom electrodes, respectively. The Ag/phos-GPs/ITO memristor switches from the initial high resistance state (HRS) to the low resistance state (LRS) upon completing the positive voltage sweep on the Ag top electrode, without the need for an electroforming process. This transition occurs at the current limit of 1 mA and direct current scanning range between -1 and +1 V, as shown in Figure 3b. Conversely, when a negative scanning voltage is applied to the silver electrode, the device consistently remains in HRS and exhibits no change in the resistance state, indicating the volatile RS behavior of the Ag/phos-GPs/ITO memristor. The *I–V* curves almost overlap and the variation coefficients of HRS and LRS at 0.2 V are calculated to quantify the state distribution (Figure 3c). The small values of 0.05 and 0.04 confirm the high stability of the volatile memristor. Furthermore, the Ag/phos-GPs/ITO memristor can maintain a relatively stable state for both HRS and LRS over 500 cycles in Figure S5 (Supporting Information), indicating the good durability of the device. In the random device-to-device test, the resistance states of ten different devices show variation coefficients of 0.21 and 0.07 for HRS and LRS, respectively (Figure 3d). In addition, Ag/phos-GPs/ITO memristors constructed by phos-GPs films with different thicknesses are conducted in Figure S6 (Supporting Information), which are not as good as the moderately-thick film. The high consistency of Ag/phos-GPs/ITO volatile memristor establishes a solid foundation for practical applications.

Since the conductance modulation ability of memristors can be used to mimic the synaptic weight change in biological synapses, the Ag/phos-GPs/ITO memristor is used to simulate the synaptic plasticity. The Ag electrode serves as the presynaptic membrane, the ITO electrode as the postsynaptic, and the conductance represents the synaptic weight. Initially, we simulate the paired pulse facilitation (PPF) and paired pulse depression (PPD) in the context of short-term synaptic plasticity (STP), which represents the synaptic enhancement or suppression response following short-term consecutive stimuli.[35,36] Particularly, the PPF behavior is conducted using two consecutive pulses with an amplitude of 0.8 V and a duration of 100 ns. The shortest and largest intervals between pulses are 1 and 6 µs, while the amplitude is changed to -0.8 V in the PPD simulation. As shown in Figure 3e,f, the PPF ratio decreases with the time interval, while the PPD ratio increases. These phenomena are consistent with the behavior of PPF and PPD of biological synapses. The relationship between the PPF and PPD behavior of the phos-GPs memristors and time interval is expressed as follows:[37]

$$\mathrm{PPF} = \frac{(G_2 - G_1)}{G_1} \times 100\% = A_1 \times e^{(-t/\tau_1)} + A_2 \times e^{(-t/\tau_2)} \quad (1)$$

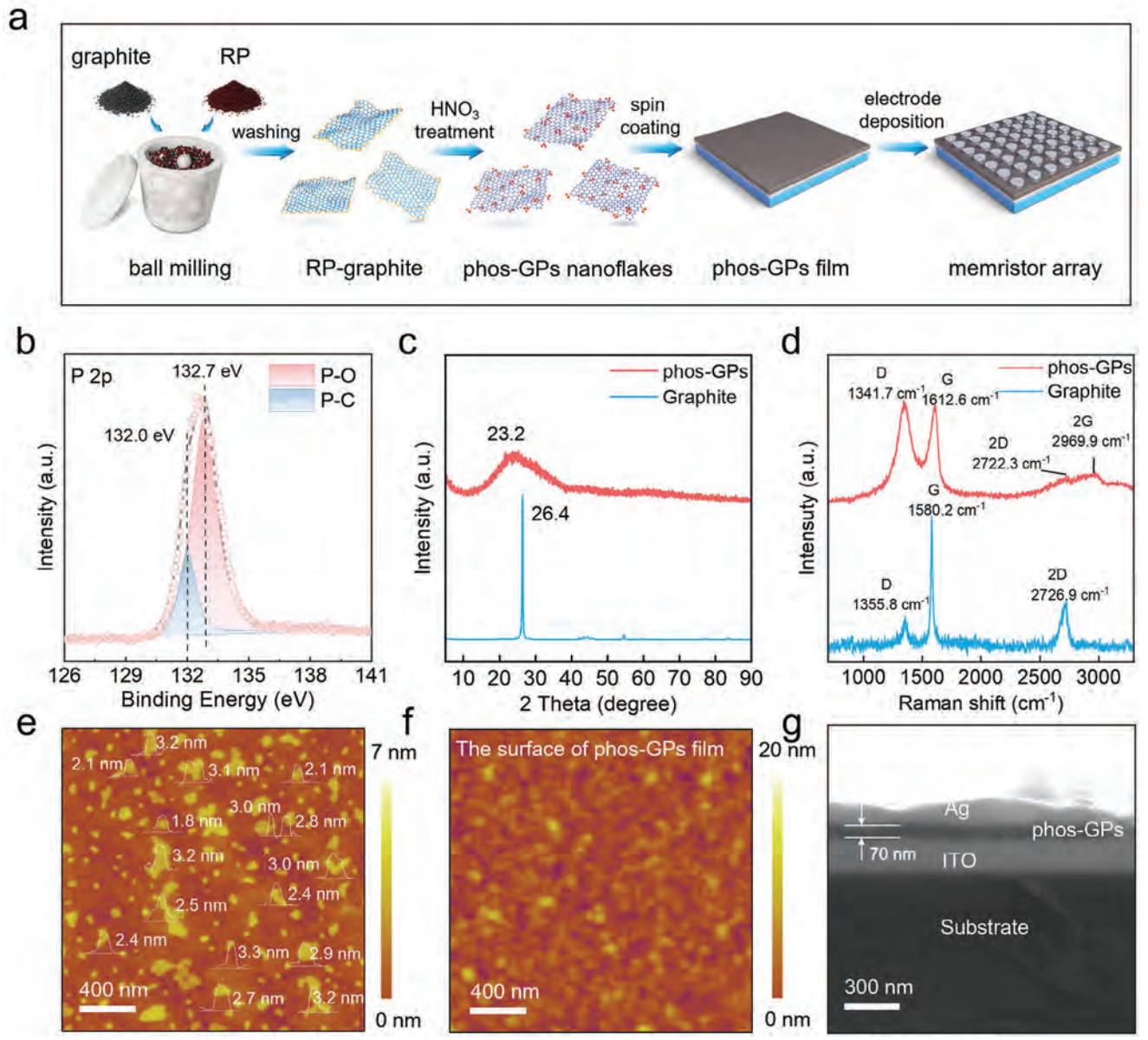

Figure 2. a) Schematic illustration of the synthesis of the phos-GPs nanoflakes and memristor; b) XPS P 2*p* spectrum of phos-GPs; c) XRD patterns and d) Raman scattering spectra of graphite and phos-GPs; AFM images of e) phos-GPs nanoflakes and f) phos-GPs film; g) cross-sectional SEM image of the phos-GPs-based memristor.

$$\mathrm{PPD} = \frac{G_2}{G_1} \times 100\% = A_1 \times e^{(-t/\tau_1)} + A_2 \times e^{(-t/\tau_2)} \quad (2)$$

where, G_2 and G_1 are the conductivities of the memristor after the first and second pulses, τ_1 and τ_2 are the two fitted time constants indicating the different rates of signal attenuation and amplification ($\tau_1 = 0.1$ ms, $\tau_2 = 2.76$ ms in PPF; $\tau_1 = 1.82$ ms, $\tau_2 = 1.83$ ms in PPD). The shorter stimulus intervals can elicit stronger conductance increase and decrease to reveal the sensitivity of conductance of the memristor in response to the stimulus intervals, which simulate the facilitation and depression characteristics of biological synapses under rapid continuous signals.

Since volatile memristors can spontaneously return to the original HRS at a read voltage, the biological learning-memory-forgetting behavior can be stimulated by the pure phos-GPs-based volatile memristor array containing 9 × 9 devices. In the test, a pulse with an amplitude of 1.0 V is applied to the electrodes to simulate the "learning" and "remember" states, while a 0.1 V read voltage is used to detect the process of slow "forgetting". The typical conductance change in Figure 3g increases with the 1.0 V stimuli and decreases with time. As shown in Figure 3h, the letter "H" is learned by 10 pulses. The letter "H" is remembered and slowly returns to the totally forgotten state. Then, the letter "T" is learned, remembered, and forgotten again. This simulation

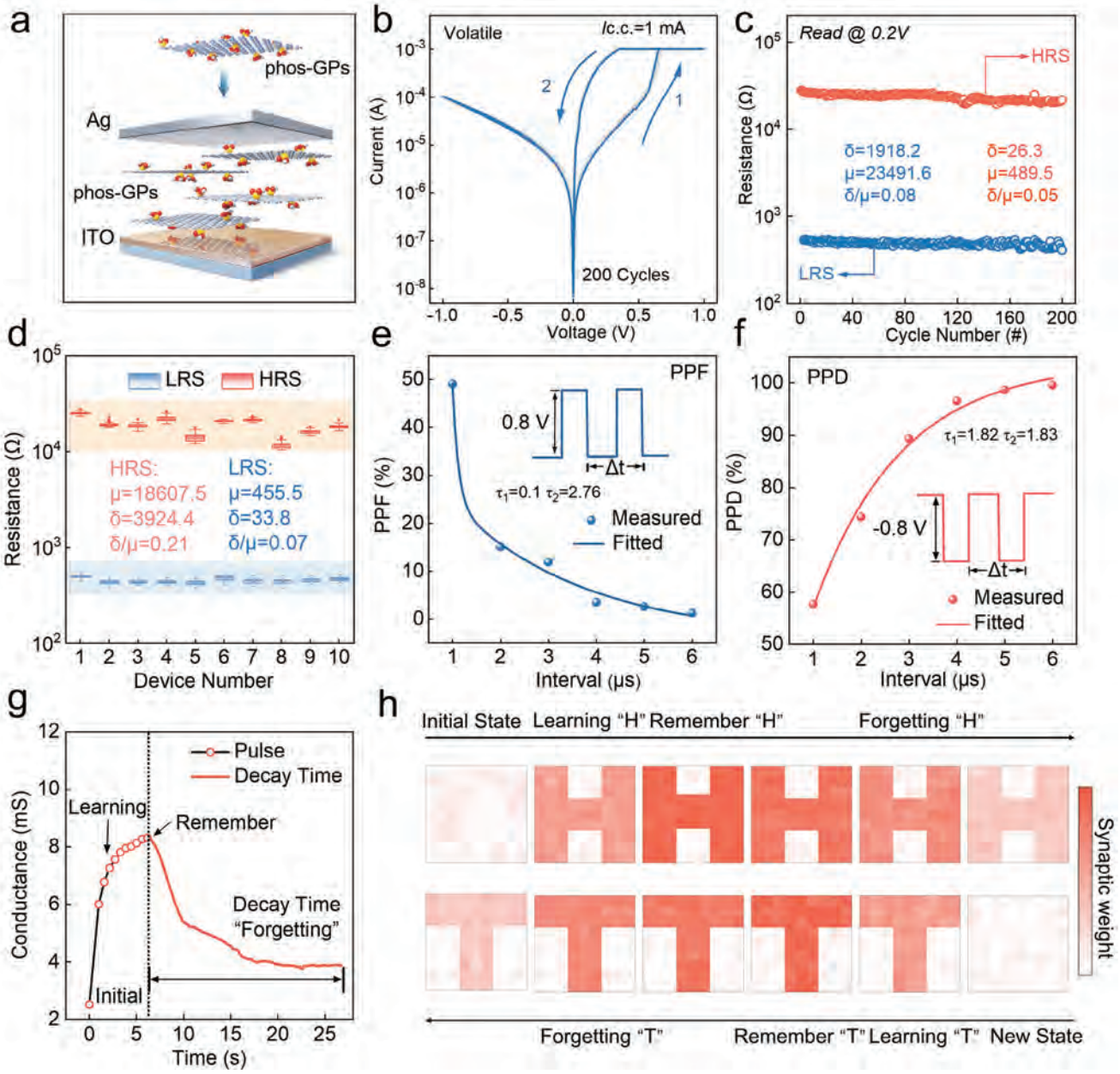

Figure 3. a) Structure of the phos-GPs-based volatile memristor (Ag/Phos-GPs/ITO); b) *I–V* curves of the phos-GPs memristor at a compliance current of 1 mA after 200 cycles; c) distribution of HRS and LRS at the 0.2 V reading voltage for 200 cycles; d) distribution of HRS and LRS of ten devices; e) PPF behavior; f) PPD behavior; g) Learning experience behavior of the pure phos-GPs-based memristor; h) learning "H" and "T" by the array containing 81 devices.

demonstrates the learning-memory-forgetting behavior of the brain.

Considering the increasing demand for flexible electronic devices, Ag/phos-GPs/ITO (PEN) flexible memristors are constructed. As shown in Figure S7 (Supporting Information), in spite of bending to different radii, the HRS and LRS are stable. The *I–V* curves obtained after 1000 bending cycles confirm the stability. These results demonstrate the excellent flexibility which can be attributed to the tightly stacked phos-GPs-based film and stable conductive channels in the RS layer.

2.3. Non-Volatile Properties of Ion-Coordinated Phos-GPs-Based Memristors

The electronegativity and polarization of phosphate groups on phos-GPs make it possible to coordinate or hybridize with metal ions like Ag^+. By dispersing phos-GPs in the aqueous $AgNO_3$ solution, positive Ag^+ ions absorb the negative phos-GPs. The XPS spectrum exhibits two strong peaks at 368.1 and 374.1 eV corresponding to Ag $3d^{5/2}$ and Ag $3d^{3/2}$, suggesting successful coordination between Ag ions and phosphate groups (Figure S8,

Supporting Information).[38,39] The uniform distribution of Ag is revealed by EDS, which also corroborates the successful introduction of silver (Figure S9, Supporting Information). The silver ion-coordinated phos-GPs is designated as Ag^+-(phos-GPs). The Ag^+-(phos-GPs) film is prepared by spin coating, and after depositing the Ag electrode, the Ag/Ag^+-(phos-GPs)/ITO memristor is built. In the *I–V* curve of the Ag^+-(phos-GPs)-based memristor (**Figure 4b**), the bias voltage is swept from −1 to +1 V and the SET process is completed at a current limit of 1 mA. Different from the pure phos-GPs-based volatile memristor, the Ag^+-(phos-GPs)-based memristor does not spontaneously return to the initial HRS after removing the electric field, and a RESET process is required to revert the device from LRS back to HRS. The observation demonstrates that the coordination with Ag^+ produces the RS behavior of the memristor and transformation from the volatile to non-volatile states. The retention times of the non-volatile memristor are measured at 300 and 340 K (Figure S10, Supporting Information). As the temperature increases, the stability of the LRS decreases, attributed to the melting of ultra-thin silver conductive filaments.[40,41] The uniformity of devices is depicted in Figures 4c and S11a (Supporting Information), the HRS and LRS distributions of twenty devices show small variation coefficients. The optical microscope images of different devices (Figure S11b, Supporting Information), with the uniform morphologies of both the film and electrode playing a key role in ensuring a high device yield. The good flexibility of the non-volatile memristor is shown in Figure S12 (Supporting Information), manifested by stable *I–V* curves for different bending radii and 1000 bending cycles.

The conductance of the memristor can be employed as synaptic weight to simulate artificial synapses. Long-term synaptic potentiation (LTP), long-term synaptic depression (LTD), PPF, and spike-timing-dependent plasticity (STDP) are mimicked on the Ag/Ag^+-(phos-GPs)/ITO memristor. In the typical LTP/LTD cycle, 50 sequential positive pulses with an amplitude of +1.0 V and a pulse width of 10 ms are applied to induce potentiation, followed by 50 consecutive negative pulses with an amplitude of −0.8 V and a pulse width of 10 ms for depression. Normalized G values is a common method to calculate the LTP and LDP nonlinearity of memristors,[42,43] as shown in Figure 4d, the nonlinearity of the fitted LTP plot is 0.381, and for the fitted LTD plot, it is 0.353. The conductance can be repeatedly modulated linearly for at least five cycles (Figures 4e and S13, Supporting Information), the modulable region is ranging from 0.5 to 3.0 mS, which is expected to be enlarged in future work. The nonlinearity of LTP and LTD is smaller than that previously published (Figure 4f; Table S2, Supporting Information), suggesting that Ag/Ag^+-(phos-GPs)/ITO memristor has great potential in neuromorphic computing.[44]

Figure S14a (Supporting Information) validates the short-term synaptic plasticity PPF behavior of non-volatile memristors. Using two pulses with an amplitude of 0.75 V and pulse width of 100 ns, the enhancing effect diminishes gradually as the pulse interval increases. Furthermore, as a classical synaptic plasticity learning rule, STDP is simulated as shown in Figure S14b (Supporting Information). During the evaluation, the top electrode and bottom electrode act as the presynaptic membrane and postsynaptic membrane, respectively. In the anti-symmetric Hebbian learning rule, the enhancement and weakening of the synaptic weight correspond to the LTP and LTP phenomena of biological synapses. In the STDP behavior of artificial synapses, the change in the synaptic weight (ΔW) is defined in the following:[45]

$$\Delta W = \frac{\left(W_{STDP} - W_0\right)}{W_0} \times 100\% \tag{3}$$

where W_{STDP} represents the conductance after the application of pulse pairs and W_0 is the conductance before the pulse pairs. When $\Delta t_{post\text{-}pre} > 0$, the device exhibits LTP. Conversely, when $\Delta t_{post\text{-}pre} < 0$, the device undergoes LTD. The following formula is used for fitting:

$$\Delta W = \begin{cases} A_+ \exp\left(-\frac{\Delta t}{\tau_1}\right), \Delta t_{post-pre} > 0 \\ -A_- \exp\left(-\frac{\Delta t}{\tau_2}\right), \Delta t_{post-pre} < 0 \end{cases} \tag{4}$$

where A_+ and A_- are the scaling factors and τ_1 and τ_2 are time constants corresponding to the response time of artificial synapses. The values of τ_1, and τ_2 for the STDP behavior are 45.93 and 111.77 ms, which approximate the response time of biological synapses and indicate high sensitivity.

After exploring the synaptic plasticity of artificial synapses, the Ag/Ag^+-(phos-GPs)/ITO non-volatile memristor is investigated for neuromorphic computing. As shown in Figure 4g, a Residual Neural Network (ResNet) is incorporated into the deep learning model. Compared to the traditional Artificial Neural Networks (ANNs), the ResNet based ANN employs a design called "jump-linking" or "constant mapping", where the input of each residual block is not only passed to the next layer, but also added directly to the output of the later layers. This design enables information to flow more efficiently and prevents information loss in the deep network. The ANN model containing input neurons, hidden neurons, output neurons, and ResNet is constructed finally. Benefiting from the continuous conductivity modulation and ultralow nonlinearity of the Ag/Ag^+-(phos-GPs)/ITO memristor, the ANN with the memristor array can complete the image recognition task for the CIFAR-10 dataset and the typical handwritten digit recognition task for the MNIST database (Figure 4h,j). After 100 training epochs, the recognition accuracy of the CIFAR-10 dataset is 81.67% and the MNIST dataset 94.72%, both of them close to the state-of-the-art performance of memristor-based ANN.[46–48] Figure 4k exhibits the confusion matrix of the 100^{th} training epochs. The recognition accuracy improves with training epochs. Therefore, the ANN composed of Ag/Ag^+-(phos-GPs)/ITO memristor has the learning ability and is effective in recognizing complex visual information.

2.4. Modulation of Volatile and Non-Volatile Resistance Switching by Silver Ions and Phosphorylation

To investigate the resistance switching mechanisms of the volatile Ag/phos-GPs/ITO memristor and non-volatile Ag/Ag^+-(phos-GPs)/ITO memristor, conductive atomic force microscopy (c-AFM) is carried out in situ to observe the growth of the conductive filaments of different memristors (**Figure 5**). In the in situ measurement, a homemade silver-coated c-AFM tip is connected to the grounding terminal, and an adjustable voltage is applied to ITO by an external power to simulate the electric field in

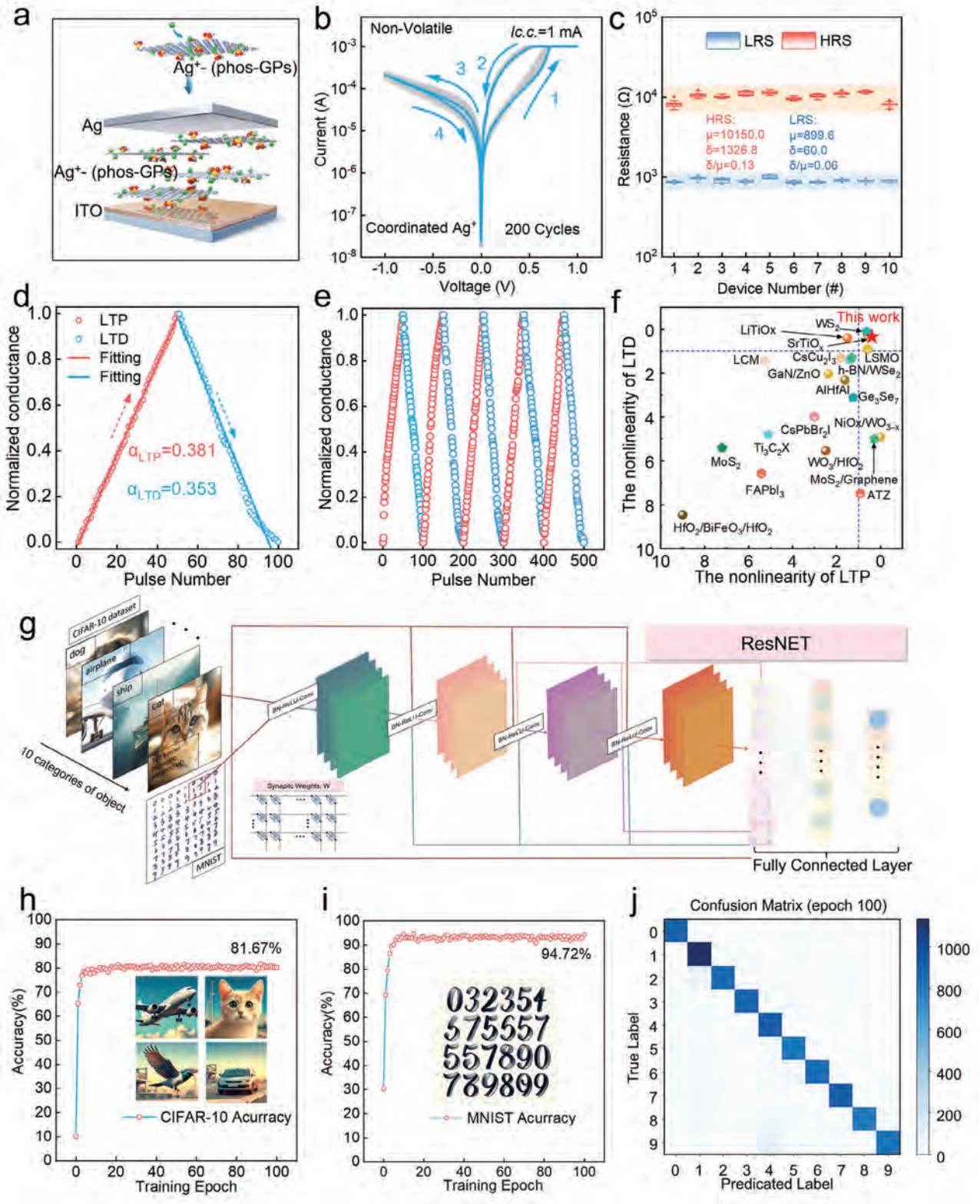

Figure 4. a) Schematic of the structure of the non-volatile Ag/Ag$^+$-(phos-GPs)/ITO memristor; b) *I–V* curves of the Ag/Ag$^+$-(phos-GPs)/ITO memristor for 200 cycles; c) HRS and LRS distributions of 10 devices; d,e) reproducible conductance modulation under repetitive potentiation and depression pulses for (d) one cycle and (e) five cycles; f) comparison of the LTD and LTP nonlinearity with previous results; g) hybrid ANN architecture of ResNet and two recognition tasks of the CIFAR-10 image dataset and MNIST handwritten digit dataset; h) recognition accuracy of the CIFAR-10 dataset; i) recognition accuracy of the MNIST dataset; j) confusion matrix plot of MNIST recognition after 100 training epochs.

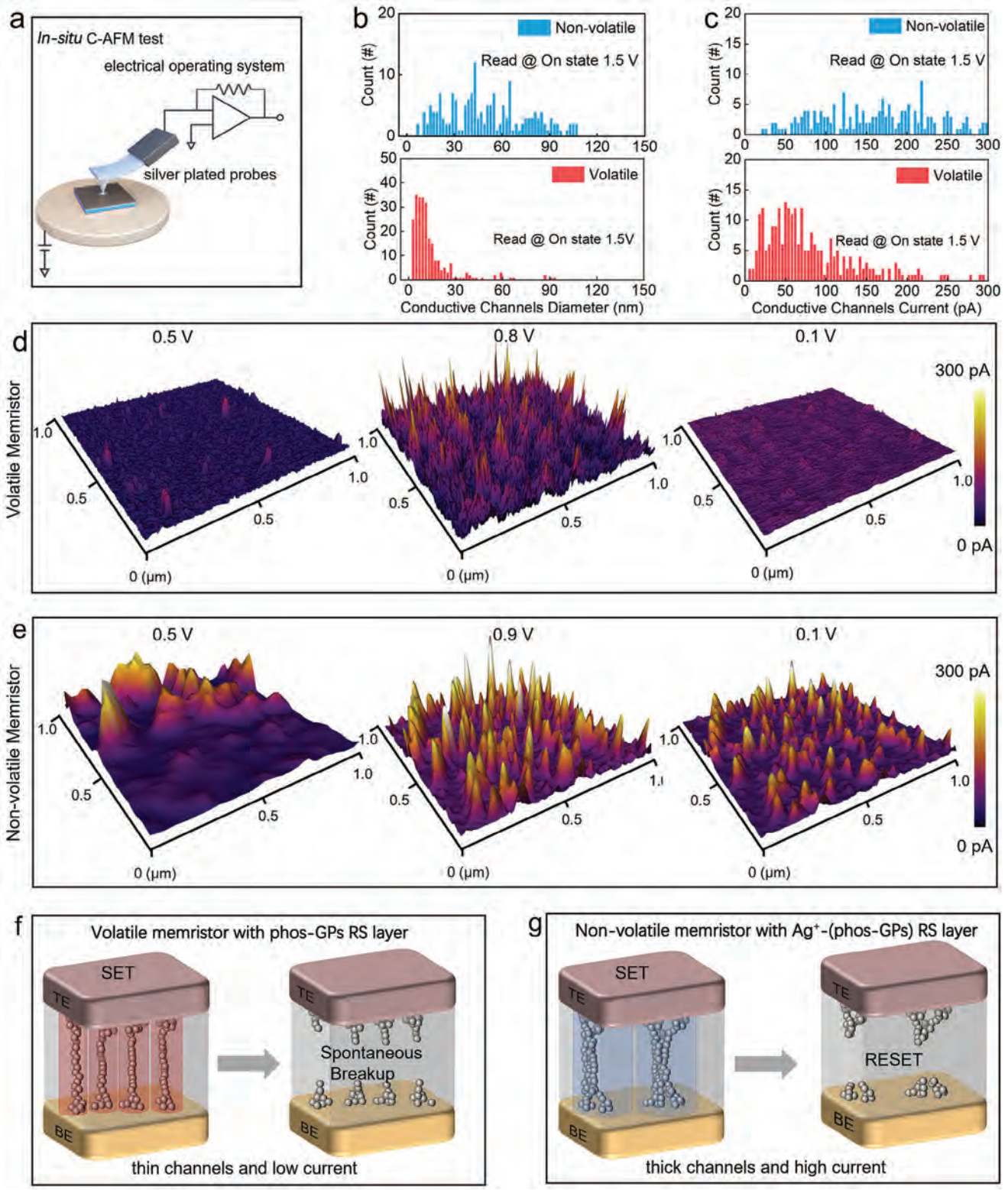

Figure 5. a) Schematic diagram of the in situ c-AFM assessment; b) diameter distribution of the conductive channels at 1.5 V; c) current intensity distribution of the conductive channels at 1.5 V; d,e) in situ c-AFM maps of d) volatile phos-GPs RS layer and e) non-volatile Ag^{+}-(phos-GPs) RS layer; f,g) schematic showing the RS mechanism of the volatile and non-volatile memristors.

the macroscopic devices (Figure 5a). In the phos-GPs film-based RS layer (Figure 5d), the weak conducting channel appears at 0.5 V, and the ultrathin and regular conductive channels emerge at 0.8 V. On account of the large surface area and small size of phos-GPs, Ag^+ ions dissolve from the silver electrode and are deposited uniformly on the RS layer to reduce the SET voltage variance. The device is read at 0.1 V without the electrical RESET process. The device returns spontaneously to its original HRS, and the conductive channel nearly disappears. Hence, the memristor comprising the phos-GPs film exhibits volatile characteristics. Compared with the volatile RS layer, the non-volatile Ag^+-(phos-GPs)-based RS layer has larger and more conducting channels at 0.5 V, as shown by the c-AFM current map in Figure 5e. When the voltage is increased to 0.9 V, the conductive channel becomes thicker. Finally, the voltage is returned to 0.1 V, and the corresponding conductive channels retain the uniform distribution, which requires a further electrical RESET process to eliminate the conductive channels, thus corroborating the non-volatile characteristics of the Ag^+-(phos-GPs)/ITO memristor. In situ C-AFM is performed throughout the entire process of the initial state, LRS, and HRS for phos-GPs/ITO and Ag+-(phos-GPs)/ITO, as shown in Figures S15 and S16 (Supporting Information).

In order to systematically compare the differences between the volatile and the non-volatile RS layers, the statistical distributions for the diameter and current intensity of the conductive channels at 1.5 V are derived. As shown in Figure 5b, the volatile conductive channel is <30 nm, but in contrast, the non-volatile Ag^+-(phos-GPs)-based RS layer has bigger channels with diameters between 30 and 120 nm. The current intensity of the Ag^+-(phos-GPs) layer is 20% bigger than that of the phos-GPs layer (Figure 5c). Since the only difference between the Ag^+-(phos-GPs) layer and the pure phos-GPs layer is the Ag^+ pre-treatment, the formation of conductive channels can be inferred to originate from coordinated Ag^+. The surface-bonded Ag^+ ions improve ion migration, facilitate filament growth, and ensure the stability of the conductive channels even after turning off the voltage.

To further elucidate the conduction mechanisms across different resistance states, Figure S17a,c (Supporting Information) present the ln(I)-ln(V) fits of the LRS curves for the volatile and non-volatile memristors. The slopes of the ln(I)-ln(V) plots of the volatile and non-volatile memristors are 1.1 and 1.2, respectively, and exhibit good linear Ohmic contact correlation, proving the formation of the conductive filament in LRS. The ln(I)-$V^{1/2}$ fitted curves of HRS for the volatile and non-volatile memristors are shown in Figure S17b,d (Supporting Information). The fitted slopes are 8.14 and 9.17, and the intercepts are −15.37 and −13.17, the absolute value of the intercept is proportional to the height of the potential barrier. The results indicate that the conductivity obeys the Schottky emission mechanism and the conductive filaments undergo varying degrees of fracture in HRS. To further investigate the Schottky emission mechanism of the memristors, the temperature-dependent I--V curves in Figure S18 (Supporting Information) show that with increasing temperature, the current in HRS increases gradually. Hence, combining in situ CAFM, the volatile and nonvolatile RS properties of the two memristors are summarized in Figure 5f,g. In the phos-GPs-based memristor, the dense and thin Ag^+ conductive filaments are melted easily by Joule heating generated during device operation.[49] Attributing to the stronger binding energy between phosphate groups and silver ions (Table S3, Supporting Information), the Ag^+ coordinates with graphene surface functionalized phosphate groups under electric field, which set up a conduction bridge to reduce the electron tunneling/hopping energy barriers.[50,51] Consequently, the Ag^+-(phos-GPs)-based memristor exhibits non-volatile characteristics.

3. Conclusion

A technique combining ball milling and oxidization is designed to synthesize phosphorylated graphene nanoflakes (phos-GPs). The small and uniform phos-GPs assemble readily into a scale-armor-like dense film, which is suitable for the flexible RS layers in memristors. By modulating the coordination between Ag^+ and phosphate functional groups in phos-GPs, the formation and kinetics of the conductive channels are altered. As a result, volatile characteristics are observed from the Ag/phos-GPs/ITO memristor, while the Ag/Ag^+-(phos-GPs)/ITO memristor exhibits non-volatility. Both memristors demonstrate consistent stability and flexibility after 100 I–V cycles and 1000 bending cycles. The volatile memristor exhibits various synaptic properties, such as PPF, PPD, STDP, and learning experience. As for the non-volatile memristor, the nonlinearity of the LTP and LTD behavior is 0.381 and 0.353, respectively, which is superior to most previous results. The excellent conductivity modulation ability makes the Ag/Ag^+-(phos-GPs)/ITO memristor an ideal candidate for constructing high-precision ANN, manifested by the high accuracy in tasks involving the recognition of MNIST handwritten digits and CIFAR-10 image datasets. This strategy of regulating conductive channels can be extended to facilitate a broader range of interactions between functional groups and metal ions, thereby opening up a new avenue for the development of neuromorphic devices.

4. Experimental Section

Preparation of Phos-GPs and Ag^+-(Phos-GPs) Dispersions: Red phosphorus (5 g) and graphite (5 g) were placed in a stainless-steel ball milling jar and in the Ar-filled glove box. The phosphorus-carbon composite was prepared by ball milling at 1500 rpm for 7 hours. The phosphorus-carbon composite (2 g) was added to 500 mL of diluted nitric acid (1:4), stirred at 80 °C for 8 hours, and kept standing overnight. The precipitate was collected and washed 2–3 times with deionized water by centrifugation at 13 000 rpm. The phos-GPs dispersion (≈10 mg mL^{-1}) was prepared for further use. The Ag^+-(phos-GPs) dispersion was synthesized by mixing the phos-GPs dispersion and $AgNO_3$ solution with a mass ratio of 200:1.

Fabrication of Volatile and Non-Volatile Memristors: The ITO/glass and ITO/PEN substrates were cleaned ultrasonically in acetone, isopropanol, and deionized water for 5 minutes each. Isopropanol was added to the phos-GPs dispersion with a volume ratio of 2:3 and stirred for 5 minutes to form the IPA/H_2O co-solvent. The co-solvent was placed on the substrate for 3 minutes, spin-coated at 200 rpm for 60 seconds and 1000 rpm for 15 seconds, and dried at room temperature. The 100 nm thick top Ag electrode was deposited on the phos-GPs film at a rate of 0.02 nm s^{-1} by masked thermal evaporation. The preparation of the non-volatile memristors was the same as that of the volatile memristors, with the exception of using the Ag^+-(phos-GPs) dispersion instead of the phos-GPs dispersion.

In Situ c-AFM: In situ c-AFM was carried out on the Cypher S AFM (Asylum Research, USA) under ambient conditions. The conductive silver probe was homemade based on the standard silicon probes (Olympus, model AC240TS) with a tip radius of <10 nm. 5 nm of chromium and

200 nm of silver were thermally evaporated onto the silicon probes at a rate of 0.02 nm s^{-1} (Shenyang Yarenfeng Technology Co., Ltd.). During the process, the probe was grounded, and the bias applied to the device was varied to collect the current-voltage data. The Avizo software was employed to combine the 2D data set into a 3D image. The process of forming set and reset states of the volatile and non-volatile memristors was characterized by c-AFM.

Materials and Device Characterization: The scanning electron microscopy (SEM) images were acquired on an Apero 2 S HiVac (Thermo Fisher, USA), and the transmission electron microscopy (TEM) and high-resolution TEM (HR-TEM) images were acquired on the JEM-F200 (JEOL, Japan). Atomic force microscopy (AFM) was performed on the Cypher S (Asylum Research, USA). Fourier transform infrared spectroscopy (FTIR) was carried out on the NICOLET is50 (Thermo Scientific, USA), and X-ray photoelectron spectroscopy (XPS) was conducted on the Escalab xi^+ (Thermo Scientific, USA).

The electrical properties including the *I–V* curves and the synaptic functions of the memory devices were measured by the pulse module with various pulse voltages on the Keithley 4200A-SCS (Keithley, USA) parameter analyzer with a pulse measurement unit (PMU) under ambient conditions.

ResNet Network Simulation: The ResNet network was constructed on a Linux server by the PyTorch framework to simulate the classification task. This network included the multiple convolutional layers, intermediate normalization and residual connection layers, and a final fully connected layer to transform the high-dimensional data into a 10-class one-hot vector, where each number represented the probability that the image belonged to that category. Here, the study chooses to execute the CIFAR-10 task recognition and MNIST database handwritten digits task recognition. After obtaining the multi-synaptic weight simulation signals of brain-like neural synapses in the real experiments, these signals were normalized, read into a JSON file, and converted into the "torchtensor" data type for subsequent use. These signals were used to initialize the convolutional layers of the network, with kernel sizes including 5 × 5, 7 × 7, etc., to extract the different image features. During the subsequent training process, these parameters were frozen to simulate the characteristics of the experimental signals.

Supporting Information

Supporting Information is available from the Wiley Online Library or from the author.

Acknowledgements

Z.Z. and Y.Q. contributed equally to this work. Financial supports were provided by the National Key R&D Program of China (2023YFA0915600), Youth Innovation Promotion Association Chinese Academy of Sciences (2020354), Young Elite Scientist Sponsorship Program by CAST (YESS20210226), Guangdong Basic and Applied Basic Research Foundation (2024A1515030176), Shenzhen Science and Technology Program (JCYJ20220818100806014), National Natural Science Foundation of China (62365010), Jiangxi Provincial Cultivation Program for Academic and Technical Leaders of Major Disciplines, https://doi.org/10.13039/501100004739 (20232BCJ23011), City University of Hong Kong (9220061 and DON-RMG 9229021) and Postdoctoral Fellowship Program of China Postdoctoral Science Foundation (GZC20241837).

Conflict of Interest

The authors declare no conflict of interest.

Data Availability Statement

The data that support the plots within this paper and other finding of this study are available from the corresponding authors upon reasonable request.

Keywords

2D materials, artificial synapses, functionalization, memristors, non-volatile, volatile

Received: September 9, 2024
Revised: November 2, 2024
Published online: November 24, 2024

[1] C. Li, M. Hu, Y. Li, H. Jiang, N. Ge, E. Montgomery, J. Zhang, W. Song, N. Dávila, C. E. Graves, Z. Li, J. P. Strachan, P. Lin, Z. Wang, M. Barnell, Q. Wu, R. S. Williams, J. J. Yang, Q. Xia, *Nat. Electron.* **2017**, *1*, 52.
[2] D. B. Strukov, G. S. Snider, D. R. Stewart, R. S. Williams, *Nature* **2008**, *453*, 80.
[3] B. Sun, Y. Chen, G. Zhou, Z. Cao, C. Yang, J. Du, X. Chen, J. Shao, *ACS Nano* **2023**, *18*, 14.
[4] P. Yao, H. Wu, B. Gao, J. Tang, Q. Zhang, W. Zhang, J. J. Yang, H. Qian, *Nature* **2020**, *577*, 641.
[5] Y. Liu, X. Zhou, H. Yan, Z. Zhu, X. Shi, Y. Peng, L. Chen, P. Chen, H. Peng, *Adv. Funct. Mater.* **2022**, *32*, 2201510.
[6] T. Wang, J. Meng, X. Zhou, Y. Liu, Z. He, Q. Han, Q. Li, J. Yu, Z. Li, Y. Liu, H. Zhu, Q. Sun, D. W. Zhang, P. Chen, H. Peng, L. Chen, *Nat. Commun.* **2022**, *13*, 7432.
[7] T. Tan, X. Jiang, C. Wang, B. Yao, H. Zhang, *Adv. Sci.* **2020**, *7*, 2000058.
[8] Q. Zhao, Z. Xie, Y.-P. Peng, K. Wang, H. Wang, X. Li, H. Wang, J. Chen, H. Zhang, X. Yan, *Mater. Horiz.* **2020**, *7*, 1495.
[9] W. Huh, D. Lee, C. H. Lee, *Adv. Mater.* **2020**, *32*, 2002092.
[10] F. Xue, C. Zhang, Y. Ma, Y. Wen, X. He, B. Yu, X. Zhang, *Adv. Mater.* **2022**, *34*, 2201880.
[11] K. Lu, X. Li, Q. Sun, X. Pang, J. Chen, T. Minari, X. Liu, Y. Song, *Mater. Horiz.* **2021**, *8*, 447.
[12] B. Tang, H. Veluri, Y. Li, Z. G. Yu, M. Waqar, J. F. Leong, M. Sivan, E. Zamburg, Y.-W. Zhang, J. Wang, A. V. Y. Thean, *Nat. Commun.* **2022**, *13*, 3037.
[13] J. Huang, S. Yang, X. Tang, L. Yang, W. Chen, Z. Chen, X. Li, Z. Zeng, Z. Tang, X. Gui, *Adv. Mater.* **2023**, *35*, 2303737.
[14] Y. Peng, N. Wang, R. Wang, Y. Cao, Y. Xin, S. Wang, T. Zeng, W. Zhang, X. Ma, Q. Feng, H. Wang, Y. Hao, *IEEE Electron Device Lett.* **2023**, *44*, 2051.
[15] P. Saha, M. Sahad E, S. Sathyanarayana, B. C. Das, *ACS Nano* **2023**, *18*, 1137.
[16] S. Bellani, A. Bartolotta, A. Agresti, G. Calogero, G. Grancini, A. Di Carlo, E. Kymakis, F. Bonaccorso, *Chem. Soc. Rev.* **2021**, *50*, 11870.
[17] S. Pazos, X. Xu, T. Guo, K. Zhu, H. N. Alshareef, M. Lanza, *Nat. Rev. Mater.* **2024**, *9*, 358.
[18] S. Ling, S. Lin, Y. Wu, Y. Li, *Chem. Eng. J.* **2024**, *486*, 150100.
[19] X. Xiong, F. Wu, Y. Ouyang, Y. Liu, Z. Wang, H. Tian, M. Dong, *Adv. Funct. Mater.* **2023**, *34*, 2213348.
[20] F. Hui, C. Zhang, H. Yu, T. Han, J. Weber, Y. Shen, Y. Xiao, X. Li, Z. Zhang, P. Liu, *Adv. Funct. Mater.* **2023**, *34*, 2302073.
[21] S. M. Hus, R. Ge, P.-A. Chen, L. Liang, G. E. Donnelly, W. Ko, F. Huang, M.-H. Chiang, A.-P. Li, D. Akinwande, *Nat. Nanotechnol.* **2020**, *16*, 58.
[22] W.-J. Sun, Y.-Y. Zhao, X.-F. Cheng, J.-H. He, J.-M. Lu, *ACS Appl. Mater. Interfaces* **2020**, *12*, 9865.
[23] M. Huang, Z. Li, H. Zhu, *Adv. Intell. Syst.* **2022**, *4*, 2200077.
[24] F. J. Romero, A. Toral-Lopez, A. Ohata, D. P. Morales, F. G. Ruiz, A. Godoy, N. Rodriguez, *Nanomaterials* **2019**, *9*, 897.
[25] A. Anouar, N. Katir, A.-S. Mamede, A. Aboulaich, K. Draoui, S. Royer, A. El Kadib, *Mater. Chem. Front.* **2019**, *3*, 242.
[26] N. R. Tanguy, J. N'Diaye, M. Arjmand, K. Lian, N. Yan, *Chem. Commun.* **2020**, *56*, 1373.

[27] L. S. K. Achary, A. Kumar, L. Rout, S. V. S. Kunapuli, R. S. Dhaka, P. Dash, *Chem. Eng. J.* **2018**, *331*, 300.
[28] E. H. Ramírez-Soria, S. García-Dalí, J. M. Munuera, D. F. Carrasco, S. Villar-Rodil, J. M. D. Tascón, J. I. Paredes, J. Bonilla-Cruz, *ACS Appl. Mater. Interfaces* **2021**, *13*, 54860.
[29] Y. Liao, M. Wang, D. Chen, *Appl. Surf. Sci.* **2019**, *484*, 83.
[30] P. Sherwood, *Surface Sci. Spectra* **2002**, *9*, 62.
[31] L. S. K. Achary, A. Kumar, L. Rout, S. V. Kunapuli, R. S. Dhaka, P. Dash, *Chem. Eng. J.* **2018**, *331*, 300.
[32] M.-J. Kim, I.-Y. Jeon, J.-M. Seo, L. Dai, J.-B. Baek, *ACS Nano* **2014**, *8*, 2820.
[33] A. C. Ferrari, J. C. Meyer, V. Scardaci, C. Casiraghi, M. Lazzeri, F. Mauri, S. Piscanec, D. Jiang, K. S. Novoselov, S. Roth, *Phys. Rev. Lett.* **2006**, *97*, 187401.
[34] D. A. Pethsangave, R. V. Khose, P. H. Wadekar, S. Some, *ACS Sustainable Chem. Eng.* **2019**, *7*, 11745.
[35] B. Mu, L. Guo, J. Liao, P. Xie, G. Ding, Z. Lv, Y. Zhou, S. T. Han, Y. Yan, *Small* **2021**, *17*, 2103837.
[36] Y. Sun, J. Li, S. Li, Y. Jiang, E. Wan, J. Zhang, Y. Shi, L. Pan, *Chip* **2023**, *2*, 100031.
[37] S. Wen, J. Li, Z. Wang, Z. Zhang, J. Zhang, *Appl. Phys. Lett.* **2023**, *123*, 043503.
[38] S. Yang, B. Xue, Y. Li, X. Li, L. Xie, S. Qin, K. Xu, Q. Zheng, *Chem. Eng. J.* **2020**, *383*, 123072.
[39] J. D. Kim, H. Yun, G. C. Kim, C. W. Lee, H. C. Choi, *Appl. Surf. Sci.* **2013**, *283*, 227.
[40] S. Menzel, U. Böttger, M. Wimmer, M. Salinga, *Adv. Funct. Mater.* **2015**, *25*, 6306.
[41] R. Wang, J.-Q. Yang, J.-Y. Mao, Z.-P. Wang, S. Wu, M. Zhou, T. Chen, Y. Zhou, S.-T. Han, *Adv. Intell. Syst.* **2020**, *2*, 2000055.
[42] P. Bousoulas, D. Sakellaropoulos, D. Tsoukalas, *Appl. Phy. Lett.* **2021**, *118*, 143502.
[43] Z. Weng, H. Zheng, W. Lei, H. Jiang, K. W. Ang, Z. Zhao, *Adv. Funct. Mater.* **2023**, *34*, 2305386.
[44] A. Frick, J. Magee, D. Johnston, *Nat. Neurosci.* **2004**, *7*, 126.
[45] R. Yang, H. M. Huang, Q. H. Hong, X. B. Yin, Z. H. Tan, T. Shi, Y. X. Zhou, X. S. Miao, X. P. Wang, S. B. Mi, *Adv. Funct. Mater.* **2018**, *28*, 1704455.
[46] Y. Wu, Q. Wang, Z. Wang, X. Wang, B. Ayyagari, S. Krishnan, M. Chudzik, W. D. Lu, *Adv. Mater.* **2023**, *35*, 2305465.
[47] D. Joksas, E. Wang, N. Barmpatsalos, W. H. Ng, A. J. Kenyon, G. A. Constantinides, A. Mehonic, *Adv. Sci.* **2022**, *9*, 2105784.
[48] Z. Wang, C. Li, P. Lin, M. Rao, Y. Nie, W. Song, Q. Qiu, Y. Li, P. Yan, J. P. Strachan, *Nat. Mach. Intell.* **2019**, *1*, 434.
[49] K. Bejtka, G. Milano, C. Ricciardi, C. F. Pirri, S. Porro, *ACS Appl. Mater. Interfaces* **2020**, *12*, 29451.
[50] V. K. Sangwan, S. V. Rangnekar, J. Kang, J. Shen, H. S. Lee, D. Lam, J. Shen, X. Liu, A. C. de Moraes, L. Kuo, *Adv. Funct. Mater.* **2021**, *31*, 2107385.
[51] J. Guo, L. Liu, B. Bian, J. Wang, X. Zhao, Y. Zhang, Y. Yan, *Nano Lett.* **2022**, *22*, 6794.

WILEY-VCH

Supporting Information

Phosphorylation Enables Nano-Graphene for Tunable Artificial Synapses

Zhenyu Zhang[1, 2, ‡], Yuanduo Qu[1, 8, ‡], Siran Chen[1, 3], Shanwu Ke[1, 4], Mengdi Hao[1, 2], Yongyue Xiao[1, 4], Shuai Zhang[1], Ziqiang Cheng,[1, 6]Jiangrong Xiao[9], Hao Huang[, 1], Cong Ye[4], Paul K. Chu[10], Xue-Feng Yu[1, 3, 5, 8], Jiahong Wang*[, 1, 3, 7, 8]*

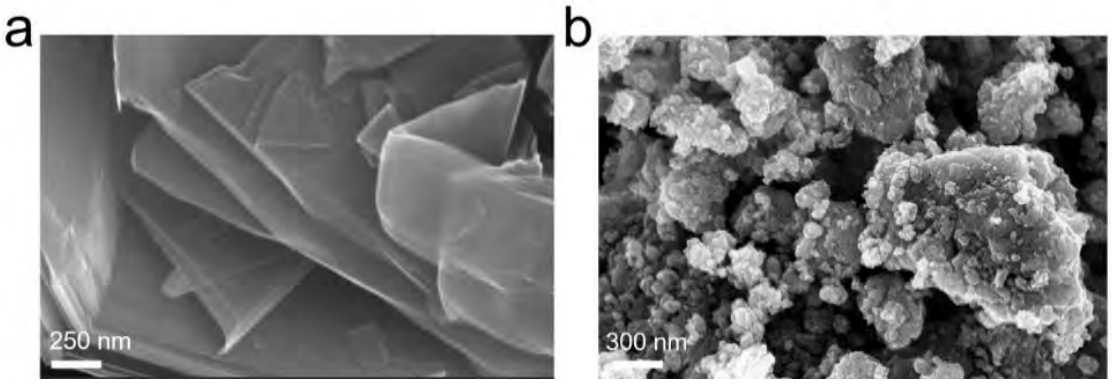

Figure S1. SEM image of (a) Pristine graphite and (b) RP-graphite.

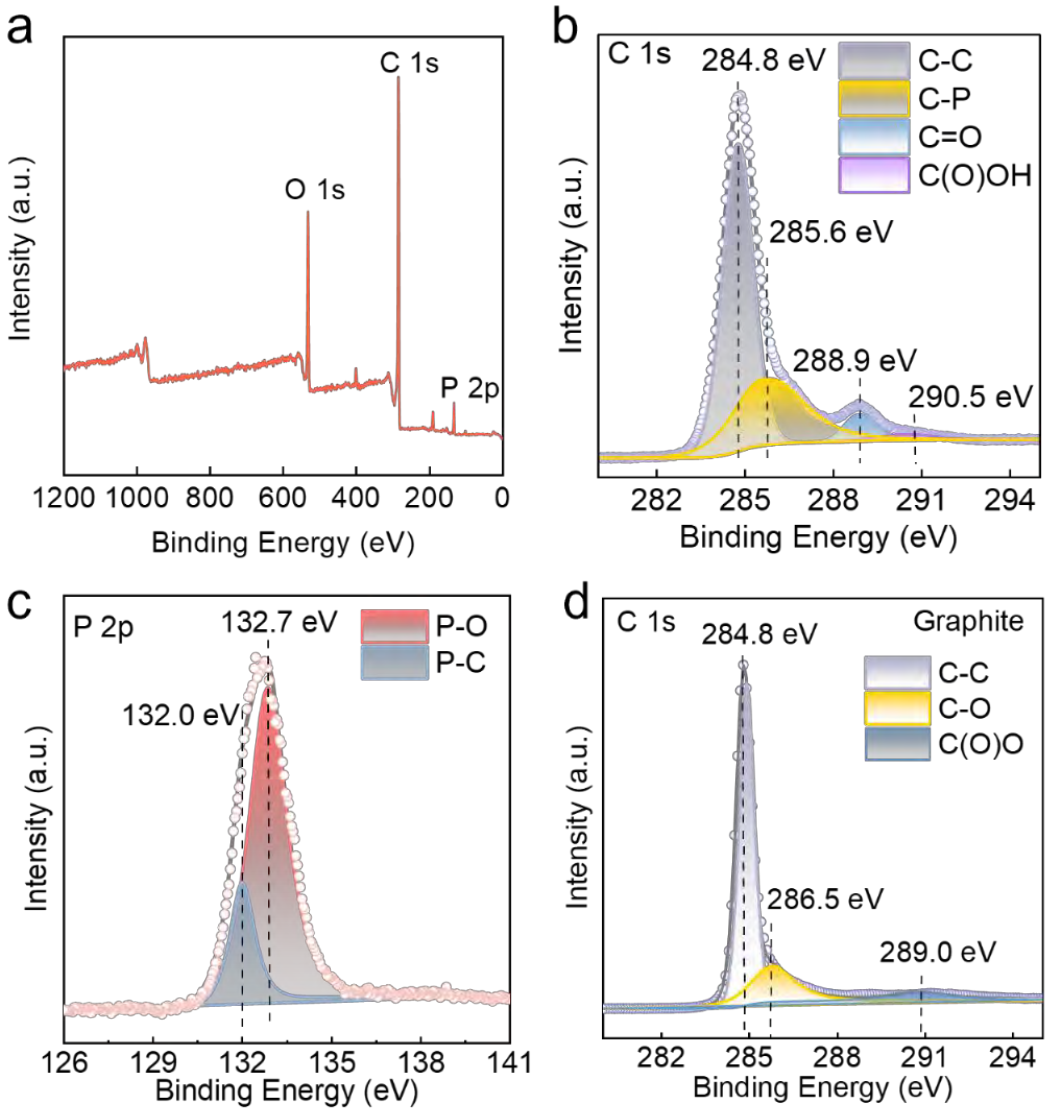

Figure S2. (a) XPS survey spectrum, (b) XPS C 1*s* spectrum, and (c) XPS P 2*p* spectrum of phos-GPs; (d) XPS C 1*s* spectrum of graphite.

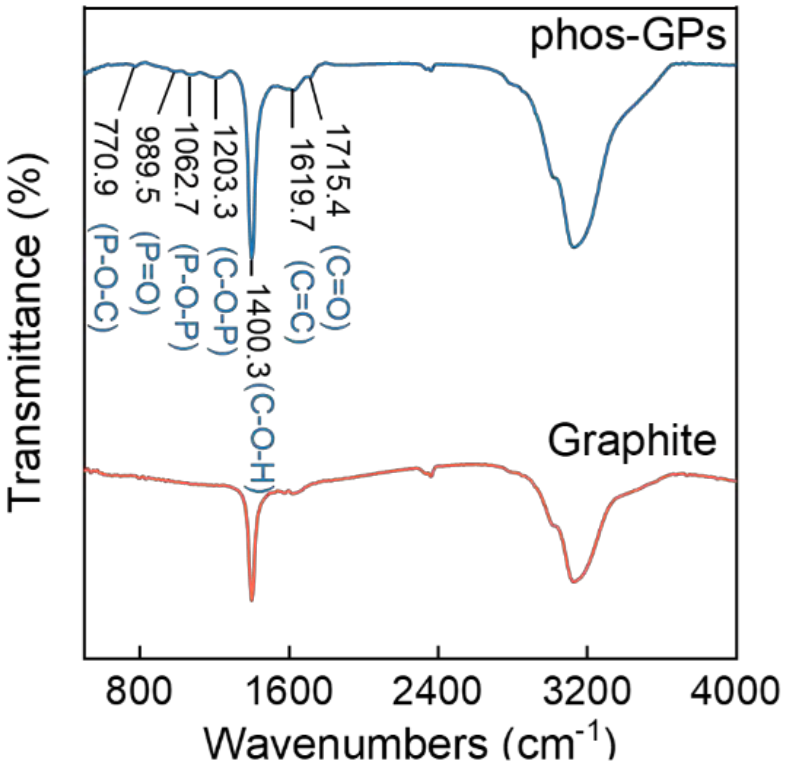

Figure S3. FTIR spectra of pristine graphite and phos-GPs.

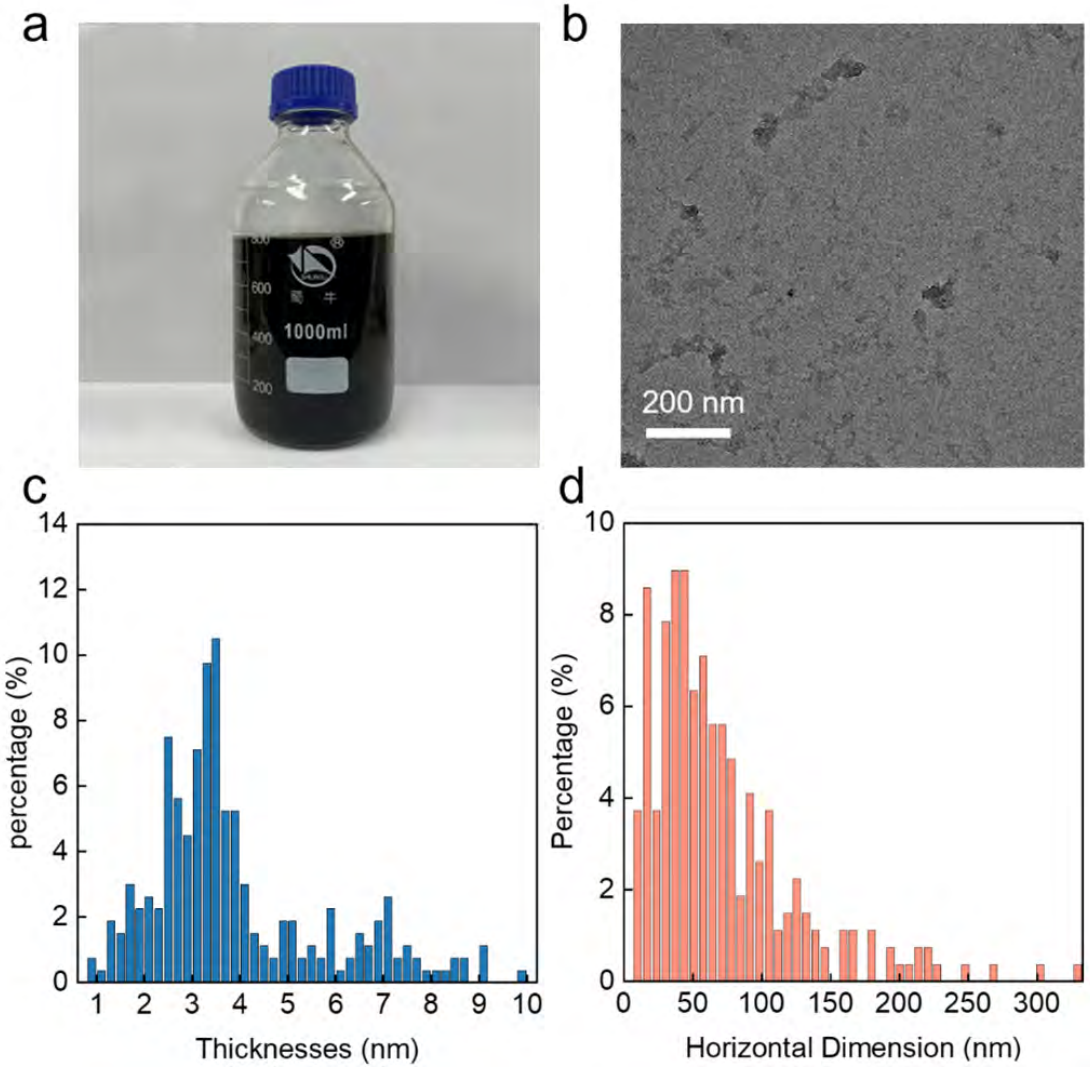

Figure S4. (a) Photograph of the phos-GPs dispersion; (b) TEM image of phos-GPs nanosheets; (c) Thickness and (d) Horizontal dimensions statistics of phos-GPs.

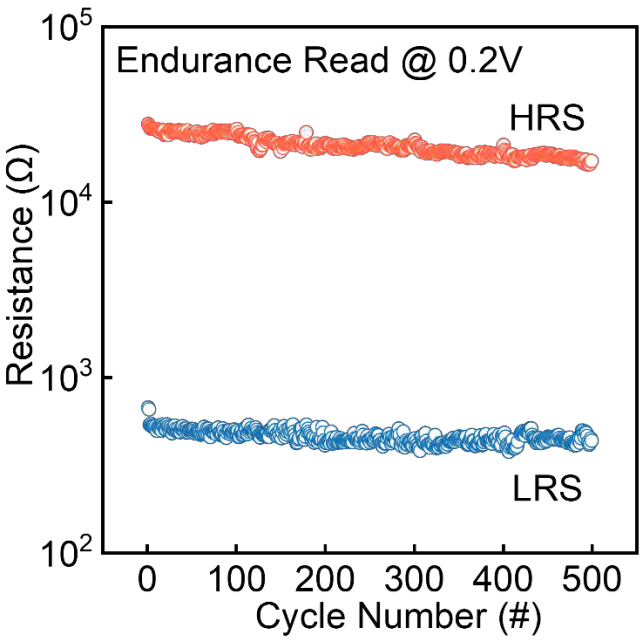

Figure S5. Resistance distributions of the volatile phos-GPs memristor in the HRS and LRS states for 500 cycles.

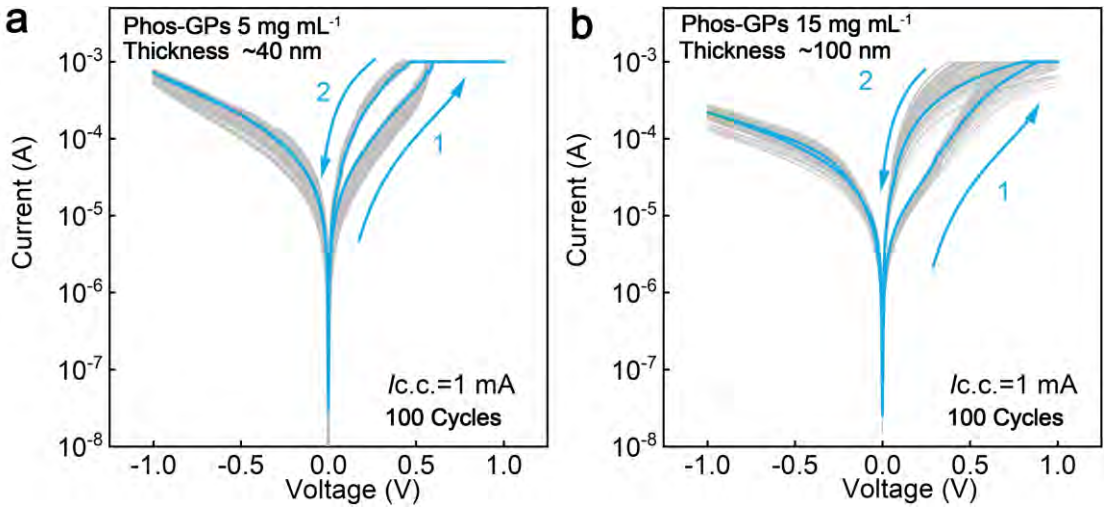

Figure S6. I-V curves of the phos-GPs memristors with different thicknesses, which are fabricated by using phos-GPs dispersion concentrations of (a) 5 mg mL^{-1} and (b) 15 mg mL^{-1}.

Both memristors show volatile characterization (**Figure S6**), however, the thin film memristor (5 mg mL^{-1}, ~ 40 nm) exhibit a smaller resistive switching window compared to the moderately thick film memristor. This difference may be attributed to the insufficient thickness of the resistive layer to impeding the growth of conductive filaments. Moreover, the thick film devices (15 mg mL^{-1}, ~ 100 nm) exhibit significantly lower consistency compared to ideal conditions, likely attributed to the loose stacking of nanoflakes.

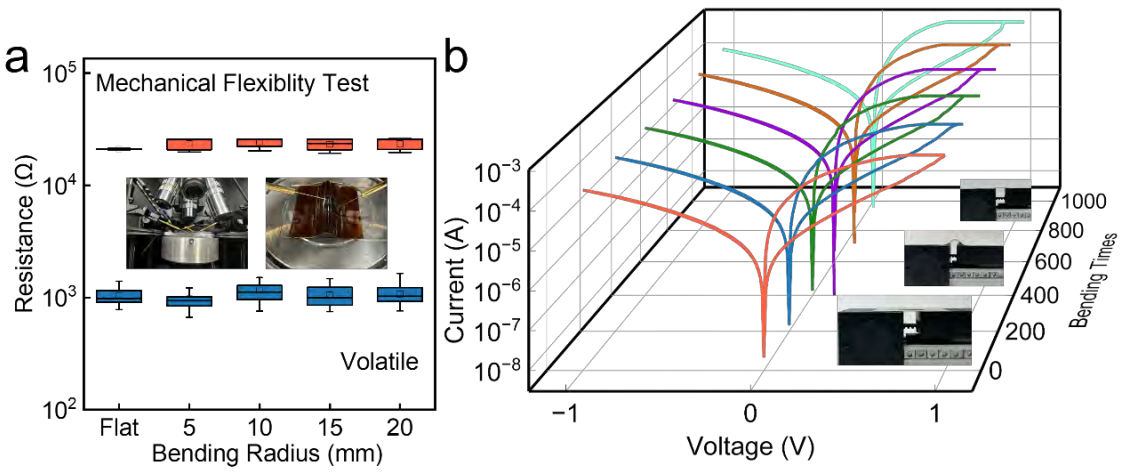

Figure S7. (a) Mechanical flexibility test of the phos-GPs memristor for different bending radii and (b) I-V curves of the memristor after 1,000 bending cycles.

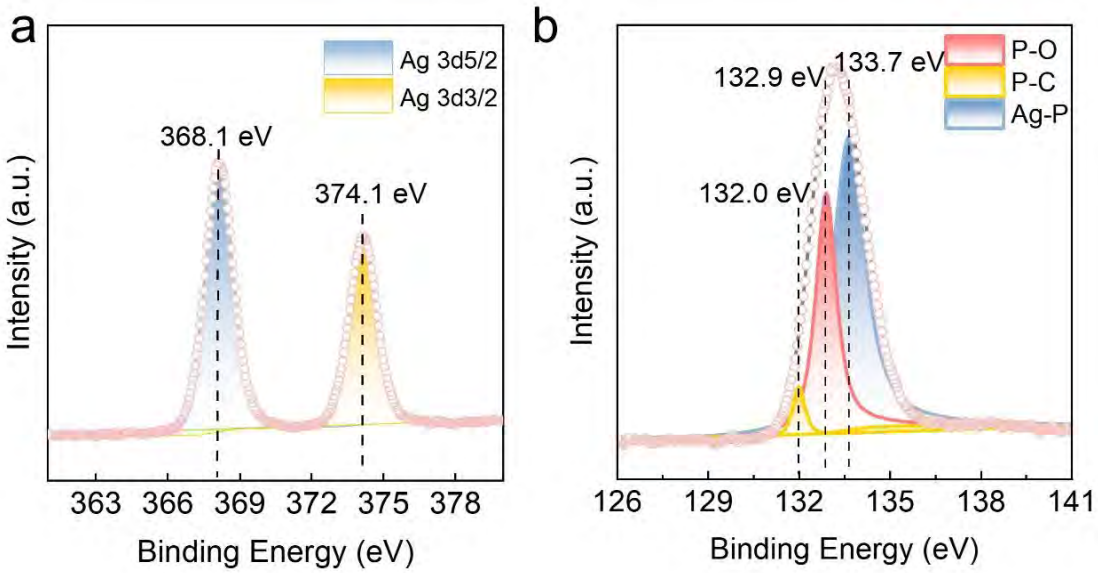

Figure S8. (a) Ag 3*d* and (b) P 2*p* XPS spectra of Ag^{+}-(phos-GPs).

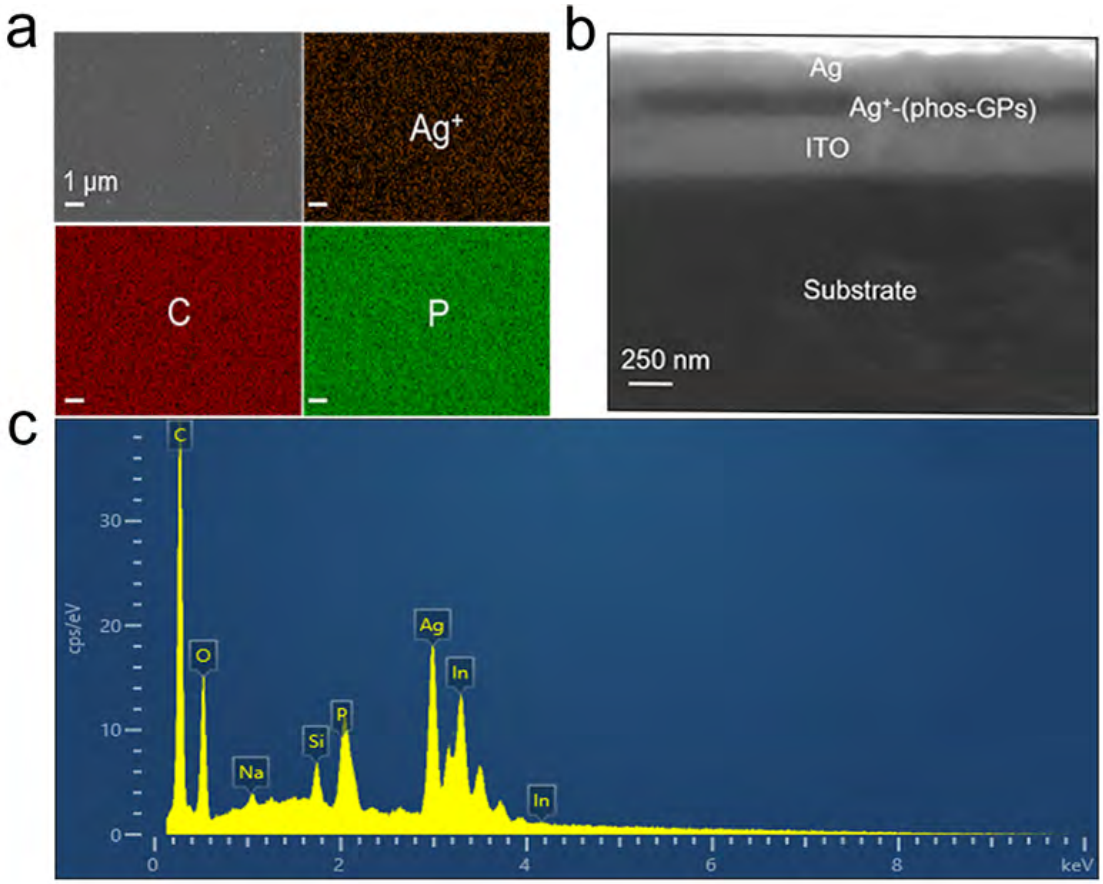

Figure S9. (a) EDS image and elemental maps of the Ag^{+}-(phos-GPs) film; (b) Cross-sectional SEM image of the Ag^{+}-(phos-GPs) memristor; (c) Elemental composition of the Ag^{+}-(phos-GPs) film. The liquid-phase coordination process is simple and does not affect the film formation while maintaining the uniformity parallel to the ITO electrode.

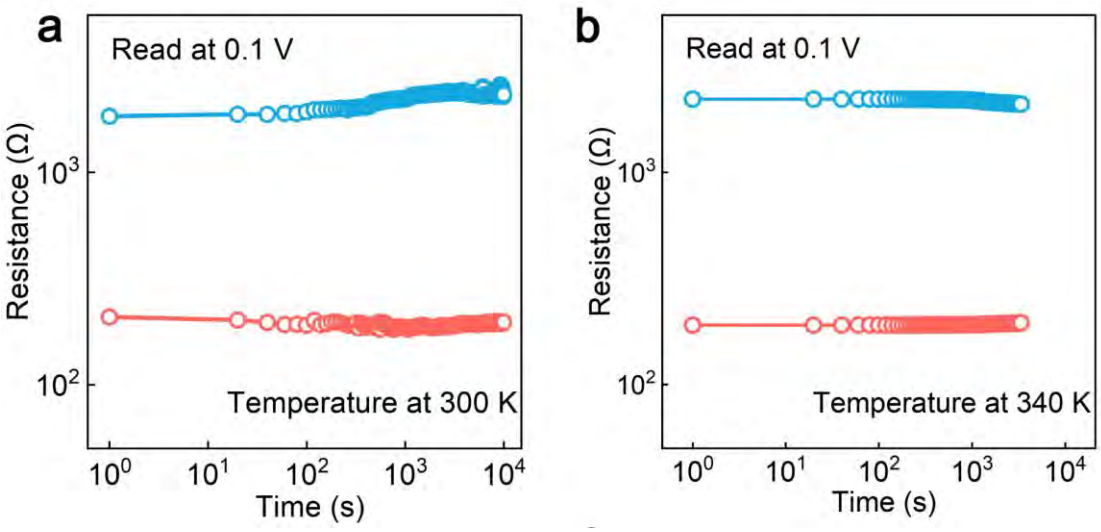

Figure S10. Retention characteristics of Ag^{+}-(phos-GPs) memristor at (a)300 K and (b) 340 K.

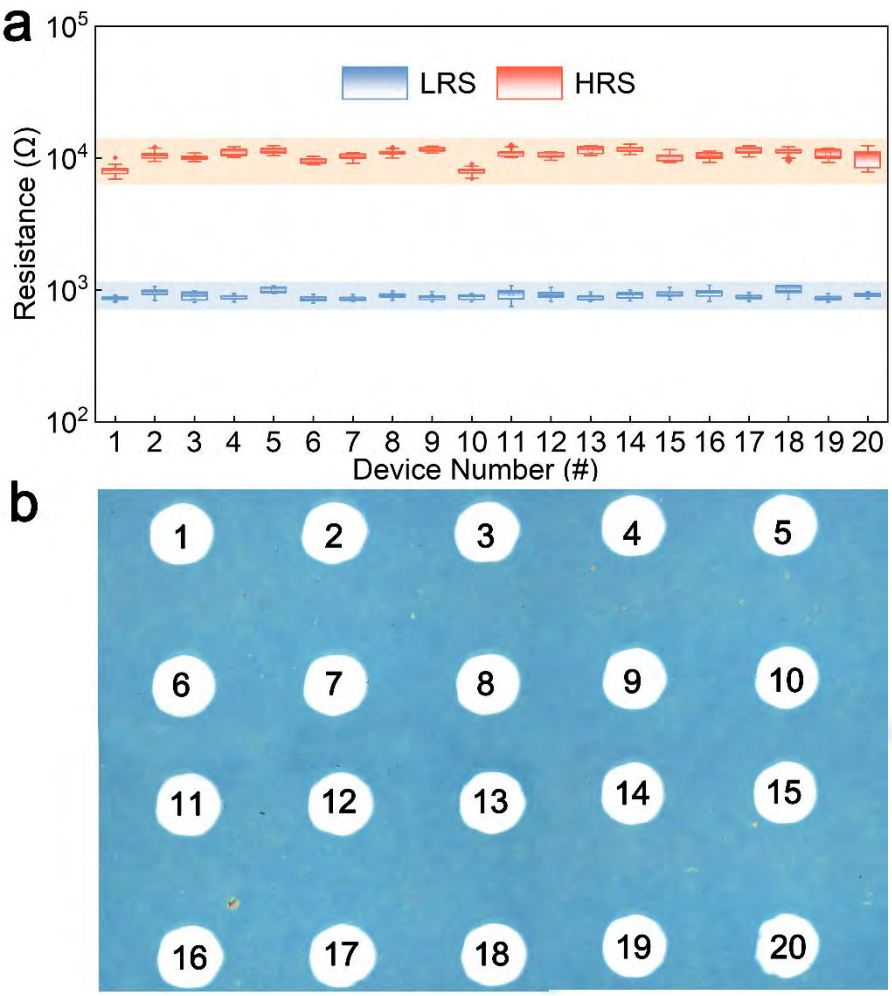

Figure S11. (a) HRS and LRS distributions and (b) optical microscope photograph of 20 Ag/Ag^{+}-(phos-GPs)/ITO memristors.

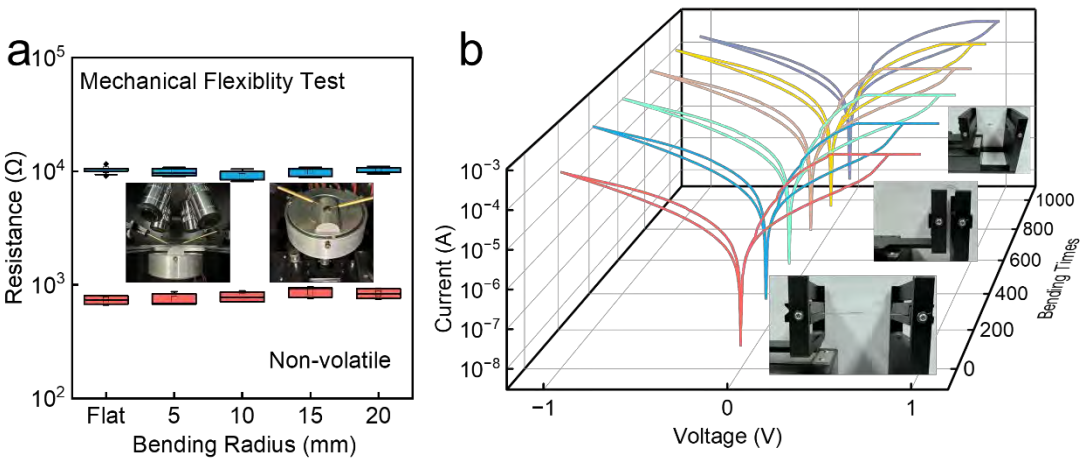

Figure S12. (a) Mechanical flexibility test of the Ag^{+}-(phos-GPs) memristor for different bending radii and (b) I-V curves of the memristor after 1,000 bending cycles.

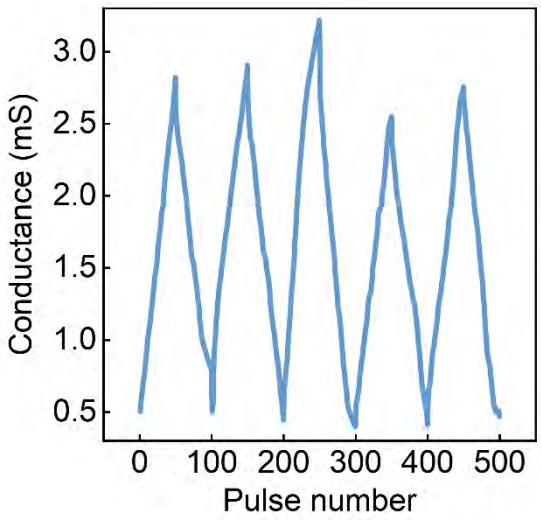

Figure S13. Original reproducible conductance modulation under repetitive potentiation and depression pulses for five cycles.

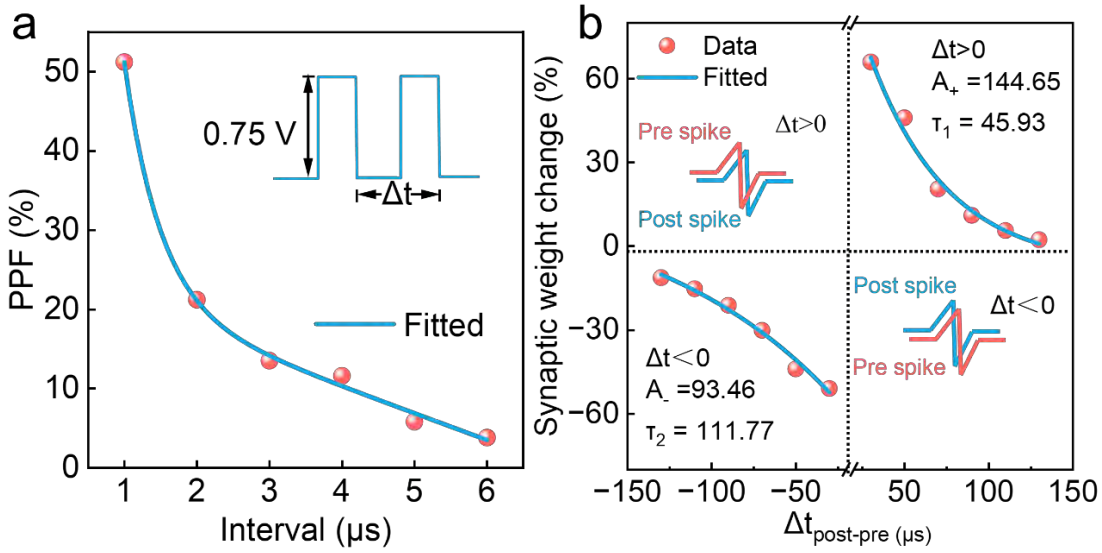

Figure S14. (a) PPF effect and (b) Asymmetric Hebbian STDP rule of the Ag^{+}-(phos-GPs) memristor.

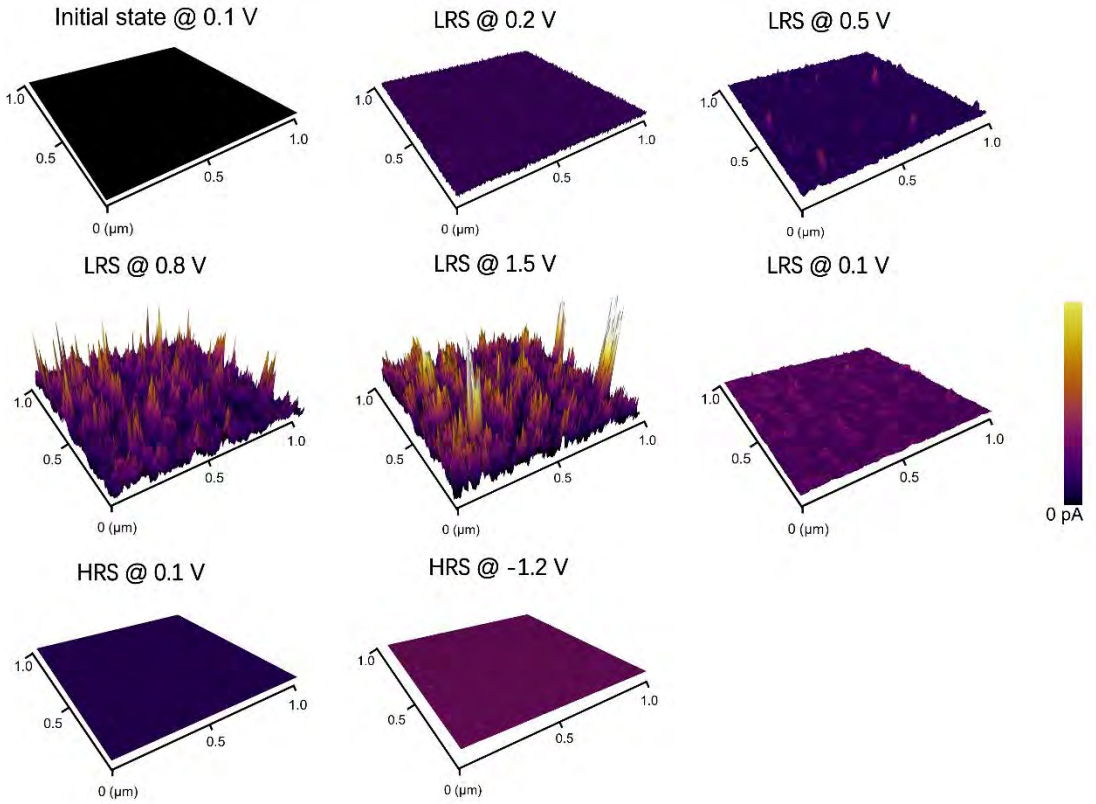

Figure S15. *In situ* C-AFM images of the volatile phos-GPs memristors.

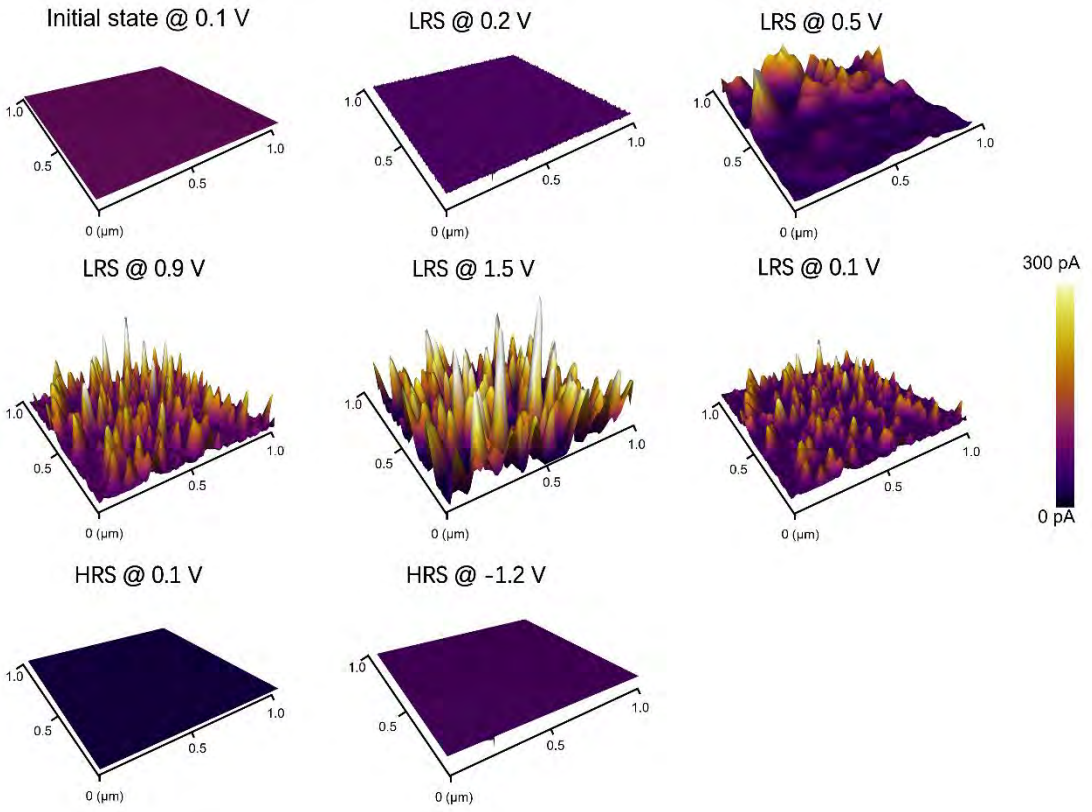

Figure S16. *In situ* C-AFM images of the non-volatile Ag^{+}-(phos-GPs) memristors.

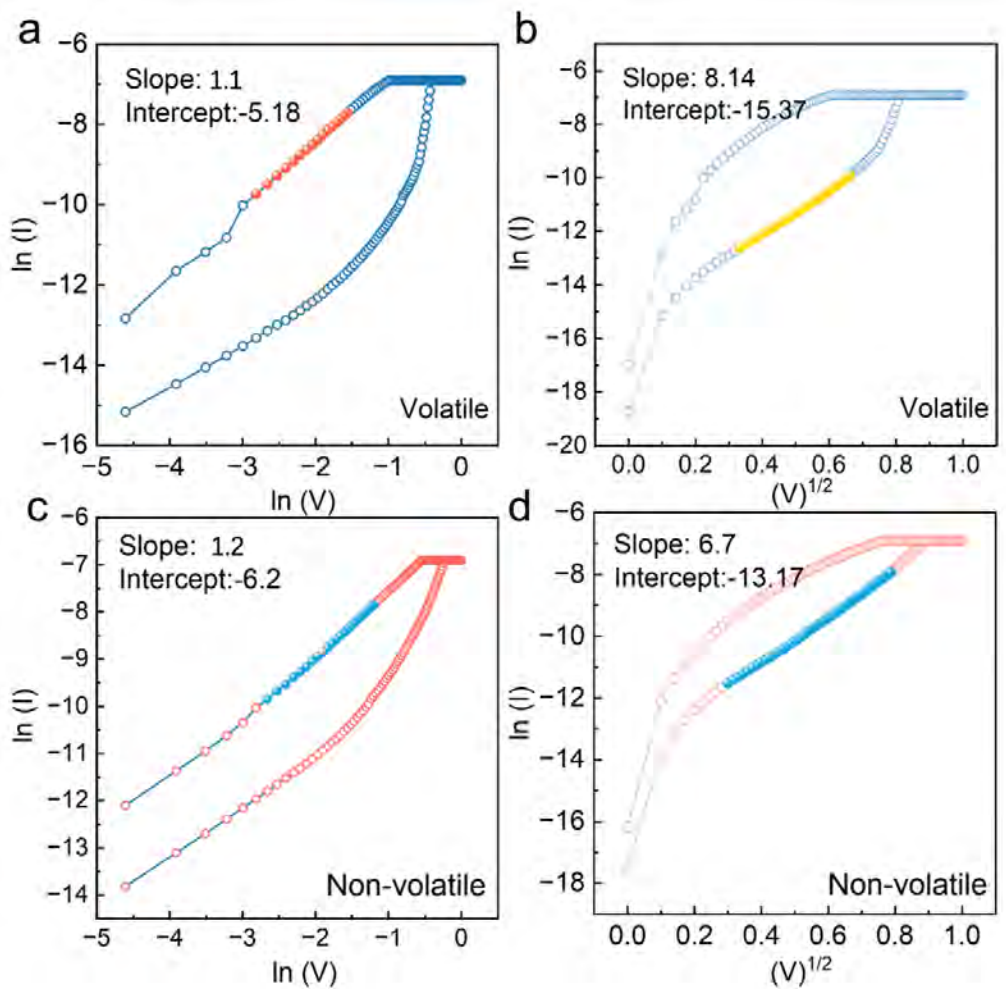

Figure S17. Fitted currents for LRS and HRS: (a-b) Volatile phos-GPs memristor and (c-d) Non-volatile Ag^{+}-(phos-GPs) memristors.

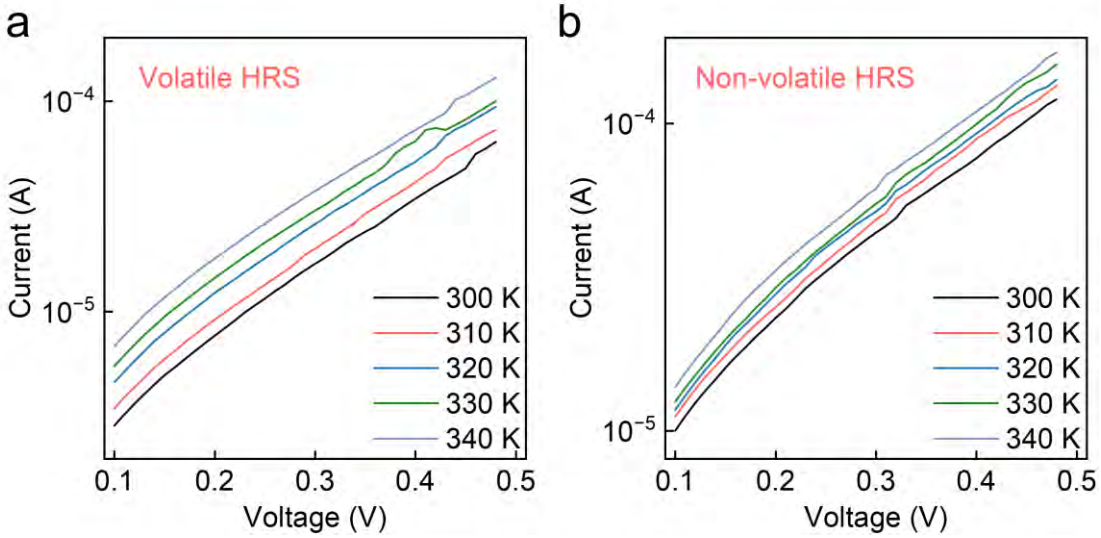

Figure S18. Temperature-dependent I-V curves for the HRS mode: (a) Volatile phos-GPs memristor and (b) Non-volatile Ag^{+}-(phos-GPs) memristor between 300 K and 340 K.

Table S1: Comparison of different preparation methods for phosphate-functionalized graphene

Method	Horizontal dimensions	Thickness	P Source	C Source	Ref.
Hydrothermal treatment	800~1000 nm	Multi layers	H_3PO_4	Graphene oxide	[25]
Arbuzov reaction	1~2 μm	Multi layers	$C_6H_{15}O_3P$	Graphene oxide	[26]
Anodic exfoliation	200~700 nm	4nm	H_3PO_4 Na_3PO_4	Graphite foil	[27]
Ball milling	50~100nm	1-4 nm	Red Phosphorus	Graphite	Our work

Table S2. Comparison of the nonlinearity of LTP and LTD of non-volatile memristors.

Device Structure	Nonlinearity ($\alpha_{LTP}/\alpha_{LTD}$)	References
Pt/NiOx/WO_{3-x}:Ti/W	0.0017 / 4.92	*Nano Letters*, 2023, 23(8): 3107-3115
Pt/h-BN/WSe_2/Ti	1.4 / 1.4	*Nature Communications*, 2018, 9(1): 5106
Ag/TiO_2NWs:ZnO QDs/FTO	0.91 / 7.49	*Nano-Micro Letters*, 2024, 16(1): 1-16
Pt/Al_2O_3(2nm)/HfO_2(10nm)/ Al_2O_3(2 nm)/Ti	1.61 / 2.31	*Nanotechnology*, 2023, 35(1): 015702
Pd/$SrTiO_3$:MgO/$La_{0.67}Sr_{0.33}MnO_3$/$SrTiO_3$/Si	0.56 / 0.34	*ACS Nano*, 2023, 17(21): 21518-21530
Ni/Au/MoS_2/graphene/Au/Ni	0.276 / 5	*Applied Physics Letters*,2019, 115(103104):1-4
TiN/ PEDOT:PSS- Li^+ /ITO	1.5 / 0.4	*IEEE Electron Device Letters*, 2022, 43(12): 2069-2072.
Ag/HTL/ $La_{0.67}Sr_{0.33}MnO_3$/ETL/ITO	0.58 / 0.91	*Science Advances*, 2022, 8(51): eade0072.
Au/P3HT/$CsPbBr_2I$/ITO	3.0 / 3.98	*Nature Communications*, 2022, 13(1): 5585.

$Ag/WO_3/HfO_2/n\text{-}Si$	2.49 / −5.54	*Advanced Materials Technologies*, 2023, 8(4): 2201143
Ti/IGZO/ZnO/Ti	0.0677 / 0.1149	*Scientific Reports*, 2022, 12(1): 1259
Ag/GaN/ZnO/ITO	2.36 / -2.03	*ACS Applied Electronic Materials*, 2022, 4(1): 297-307.
$Pt/HfO_2/BiFeO_3/HfO_2/TiN$	9 / 8.46	*Advanced Functional Materials*, 2021, 31(48): 2107131.
$Au/Al{:}TiO_x/Ti$	0.46 / 0.3	*Physica Status Solidi (a)*, 2024, 221(6):2300827
$Pt/Cu\text{-}Ge_3Se_7/TiN/W$	1.243 / 3.126	*Advanced Materials*, 2022, 34(40): 2203643
$Pt/BaTiO_3$ $(La_{0.67}Sr_{0.33})$ $/MnO_3$ / $SrTiO_3$	0.91 / 0.58	*Journal of Applied Physics*, 2023, 133(044502):1-10
$Au/FAPbI_3/SnO_2/ITP$	5.41 / 6.58	*SmartMat*, 2023: e1233
$Ag/MoO_x/RbPbI_3/ITO$	0.312 / −0.26	*ACS Energy Letters*, 2024, 9(3): 948-958
$Au/CsCu_2I_3/ITO$	1.8 / 1.3	*Nano Letters*, 2022, 22(14): 6010-6017
$Ag/WS_2/Ag$	0.63 / 0.1	*NPJ 2D Materials and Applications*, 2023, 63:1-12
$Au/MoS_2/Au$	1.4 / 1.4	*IScience,* 2020, 23(11): 101676

$Pt/Li_7Pt_5O_{12}/Pt$	5.25 / 1.45	*ACS Applied Materials & Interfaces,* 2022, 14(4): 5673-5681
Ag/Ag^+-(phos-GPs)/ITO	0.381/0.353	This work

Table S3: Comparison of binding energy between different functional groups and silver ions

Functional group	Binding energy with Ag^+ (eV)
$-NH_2$	-4.652
-COOH	-3.098
$-PO_4$	-6.829

The detail of DFT calculations: The Vienna Ab Initio Package was used to conduct density functional theory calculations using the generalized gradient approximation based on the Perdew, Burke, and Ernzerhof (PBE) formulation. Partial occupancies of the Kohn-Sham orbitals were permitted through the Gaussian smearing method with a width of 0.05 eV. The electronic energy was deemed self-consistent when the energy variation was below 10^{-5} eV. Geometry optimization was considered to converge when the force variation was less than 0.03 eV/Å. The DFT-D3 method developed by Grimme was utilized to account for van der Waals forces. The equilibrium lattice constants were refined using a $3\times3\times1$ Monkhorst-Pack k-point grid to sample the Brillouin zone. The vacuum separation perpendicular to the structural plane was set

at 20 Å. Finally, the adsorption energies (E_{ads}) were calculated using the equation $E_{ads}=E_{ad/sub}-E_{ad}-E_{sub}$, where $E_{ad/sub}$ represents the total energy of the optimized adsorbate/substrate system, Ead denotes the energy of the adsorbate in the structure, and E_{sub} refers to the energy of the clean substrate.